

1 **Zebrafish *Dscaml1* is Essential for Retinal Patterning and Function of**
2 **Oculomotor Subcircuits**

3

4 Manxiu Ma^{1,2#}, Alejandro D. Ramirez^{3#}, Tong Wang^{1#}, Rachel L. Roberts^{1,4}, Katherine E. Harmon⁵,
5 David Schoppik⁵, Avirale Sharma¹, Christopher Kuang^{1,6}, Stephanie L. Goei⁷, James A. Gagnon^{8,9},
6 Steve Zimmerman⁸, Shengdar Q. Tsai^{10,11,12}, Deepak Reyon^{10,11,13}, J. Keith Joung^{10,11}, Emre R. F.
7 Aksay³, Alexander F. Schier^{8,14}, and Y. Albert Pan^{1,2*}

8

9 ¹Department of Neuroscience and Regenerative Medicine, Medical College of Georgia, Augusta University,
10 Augusta, GA 30912.

11 ²Center for Neurobiology Research, Fralin Biomedical Research Institute at Virginia Tech Carilion, Virginia
12 Tech, VA 24016.

13 ³Institute for Computational Biomedicine and the Department of Physiology and Biophysics, Weill Cornell
14 Medical College, New York, New York 10021.

15 ⁴Graduate Program in Neuroscience, Augusta University.

16 ⁵Depts. of Otolaryngology, Neuroscience & Physiology, and the Neuroscience Institute, New York University
17 Langone School of Medicine, New York, NY 10016.

18 ⁶Medical Scholars Program, Augusta University.

19 ⁷Department of Ophthalmology, Medical College of Georgia, Augusta University, Augusta, GA 30912

20 ⁸Department of Molecular and Cellular Biology, Harvard Stem Cell Institute, Center for Brain Science,
21 Harvard University, Cambridge, MA 02138.

22 ⁹Current address: School of Biological Sciences, University of Utah, Salt Lake City, Utah 84412

23 ¹⁰Molecular Pathology Unit, Center for Computational and Integrative Biology, and Center for Cancer
24 Research, Massachusetts General Hospital, Charlestown, MA 02129.

25 ¹¹Department of Pathology, Harvard Medical School, Boston, MA 02115.

26 ¹²Current address: Department of Hematology, St. Jude Children's Research Hospital, Memphis, TN, 38105.

27 ¹³Current address: Editas Medicine, 11 Hurley Street, Cambridge, MA 02142.

28 ¹⁴The Broad Institute of Massachusetts Institute of Technology and Harvard, Cambridge, MA 02142.

29 #T.W., M.M., and A.R. contributed equally to this article.

30

31 *Correspondence should be addressed to Y. Albert Pan, Center for Neurobiology Research, Fralin
32 Biomedical Research Institute at VTC, 2 Riverside Circle, Roanoke, VA 24016. E-mail:yapan@vtc.vt.edu.

33

34 **Conflict of Interest:** J.K.J. has financial interests in Beam Therapeutics, Editas Medicine, Pairwise Plants,
35 Poseida Therapeutics, Transposagen Biopharmaceuticals, and Verve Therapeutics. J.K.J.'s interests were
36 reviewed and are managed by Massachusetts General Hospital and Partners HealthCare in accordance with
37 their conflict of interest policies. J.K.J. holds equity in Excelsior Genomics. J.K.J. is a member of the Board of
38 Directors of the American Society of Gene and Cell Therapy. J.K.J. is a co-inventor on various patents and
39 patent applications that describe gene editing and epigenetic editing technologies.

40

41 **Abstract**

42 Down Syndrome Cell Adhesion Molecules (*dscam* and *dscaml1*) are essential regulators of neural
43 circuit assembly, but their roles in vertebrate neural circuit function are still mostly unexplored. We
44 investigated the role of *dscaml1* in the zebrafish oculomotor system, where behavior, circuit
45 function, and neuronal activity can be precisely quantified. Loss of zebrafish *dscaml1* resulted in
46 deficits in retinal patterning and light adaptation, consistent with its known roles in mammals.
47 Oculomotor analyses showed that mutants have abnormal gaze stabilization, impaired fixation,
48 disconjugation, and faster fatigue. Notably, the saccade and fatigue phenotypes in *dscaml1* mutants
49 are reminiscent of human ocular motor apraxia, for which no animal model exists. Two-photon
50 calcium imaging showed that loss of *dscaml1* leads to impairment in the saccadic premotor pathway
51 but not the pretectum-vestibular premotor pathway, indicating a subcircuit requirement for
52 *dscaml1*. Together, we show that *dscaml1* has both broad and specific roles in oculomotor circuit
53 function, providing a new animal model to investigate the development of premotor pathways and
54 their associated human ocular disorders.

55

56 **Introduction**

57 The Down Syndrome Cell Adhesion Molecule (DSCAM) family proteins are neuronal cell recognition
58 molecules that are essential for neural circuit assembly and neural patterning across different phyla.
59 In humans, loss of DSCAM and DSCAM-like 1 (DSCAML1) are linked to autism spectrum disorder
60 and cortical abnormalities^{1,2}. At the cellular level, DSCAMs promote avoidance between neurites of
61 the same cell or between similar cell types. DSCAMs are also involved in the regulation of cell death,
62 synaptic adhesion, axon outgrowth, axonal refinement, and dendritic growth^{3,4,5,6,7,8}. However, it
63 is still unclear how the sum of these cellular functions contribute to neural circuit activity, behavior,
64 and human disorders.

65 Here, we investigate the role of DSCAML1 on neural circuit function in the context of oculomotor
66 behavior, a setting with a rich history and easy to quantify behaviors. Eye movement is an integral
67 part of visual perception and survival in vertebrates, enabling shifts in visual attention and

68 preventing image blurring during object or head motion. We focus on saccade, fixation, and gaze
69 stabilization movements, which are highly conserved among vertebrates. Saccades are fast ballistic
70 eye movements that allow rapid gaze shifting and redirection of visual attention. After each saccade,
71 gaze is maintained at a single location, termed fixation. Saccades also occur reflexively during gaze
72 stabilization, *e.g.*, the optokinetic reflex (OKR) and vestibular ocular reflex (VOR)⁹. OKR is triggered
73 by broad-field visual motion, during which the eyes counteract motion by velocity-matched eye
74 movements. The periods of velocity matching, called 'slow phase', are interrupted by 'fast phase'
75 saccadic movements to the opposite direction, which reset eye position. Slow and fast phases are
76 also triggered by the vestibular system in the VOR to counteract head motion.

77 In the oculomotor system, the neural circuitry is mapped in detail, and changes to eye movement
78 kinematics can be attributed to specific subcircuit deficits. Sensory inputs and motor commands
79 from higher brain centers converge onto the brainstem, where premotor neurons generate motor
80 signals encoding eye position and velocity. The premotor pathways, in turn, activate the cranial
81 motor neurons that innervate the extraocular muscles (Fig. 1A). Three subcircuits are the focus of
82 this study. The saccadic premotor pathway, which goes through the excitatory burst neurons in the
83 midbrain and hindbrain, initiates saccade and encodes the appropriate eye velocity. The vestibular
84 premotor pathway, which receives input from the eye and ear, controls slower eye movement and
85 velocity matching during gaze stabilization. Lastly, the neural integrator premotor pathway
86 integrates information from the saccade and vestibular pathways to maintain stable eye position
87 over time. Deficits in these subcircuits are associated with human diseases such as ocular motor
88 apraxia (saccade deficit), optokinetic response abnormalities (vestibular deficit), and gaze-evoked
89 nystagmus (neural integrator deficit)⁹. Eye movement deficits are common in the general
90 population and can lead to severely impaired visual function and difficulty in daily tasks such as
91 reading or crossing the street. Saccade deficits are also highly prevalent in neuropsychiatric and
92 neurodegenerative patient populations, serving as a diagnostic tool and a window into the
93 underlying pathophysiology^{10, 11}. However, our understanding of the genetic contributors for
94 oculomotor circuit development and neural mechanisms for eye movement disorders are still
95 limited.

96 We take advantage of the zebrafish oculomotor system as a framework to probe the role of *dscaml1*,
97 the zebrafish homolog of *DSCAML1*, in neural circuit development, neuronal activity, and behavior
98 ¹². Zebrafish oculomotor behavior is robust at the larval stage; the small size and optically
99 translucency of zebrafish larvae make it possible to use two-photon calcium imaging to record
100 neuronal activity *en masse* while the animal is behaving ¹³. Additionally, the ontogeny and anatomy
101 of the fish oculomotor system is well characterized and conserved with that of mammals ^{14, 15}. We
102 found that genetic deletion of zebrafish *dscaml1* affected retinal patterning, light adaptation, and
103 oculomotor behaviors. Our results suggest that for horizontal eye movements, the saccade and
104 integrator subcircuits are affected in *dscaml1* mutants, while the vestibular subcircuit is mostly
105 spared. *dscaml1* also affects the robustness of OKR against prolonged visual stimulation. The mutant
106 phenotype mirrors several characteristic features of congenital ocular motor apraxia (COMA)
107 (OMIM 257550) and provides insight into the potential neural mechanisms of COMA and other
108 human oculomotor disorders ^{16, 17}.

109 **Results**

110 To investigate the role of *dscaml1* in visual circuit activity and function, we first examined its
111 expression in zebrafish. Then we assessed how the loss of *dscaml1* affected visual pathway
112 development and locomotor behavior. Finally, we analyzed oculomotor behavior and neural activity
113 to deduce the underlying neural circuit changes in *dscaml1* mutants.

114 **Expression and gene targeting of zebrafish *dscaml1***

115 We examined the expression of *dscaml1* with whole-mount fluorescent *in situ* hybridization, from
116 the embryonic stage to five days post-fertilization (dpf), during which visually guided eye
117 movements begin to mature ^{18, 19}. *dscaml1* expression was enriched in the nervous system and
118 present in most brain regions (Fig. 1B-E). In the retina, *dscaml1* was expressed in the inner nuclear
119 layer (INL, containing the amacrine, bipolar, and horizontal cells) and the ganglion cell layer (GCL,
120 containing retinal ganglion cells and amacrine cells) at 3 dpf (Fig. 1F-G). At 5 dpf, *dscaml1*
121 expression was seen predominantly in the INL and sparsely in the GCL. These early and late

122 expression patterns match the expression of mouse *Dscaml1* in the retina at P6 and P12,
123 respectively^{12, 20}.

124 To test the function of *dscaml1*, we generated a mutant allele of *dscaml1* by TAL-like effector
125 nucleases (TALENs) mediated gene targeting²¹. The mutant allele, *dscaml1^{vt1}*, contains a seven base
126 pair deletion (9 base pair deletion plus 2 base pair insertion) after the start codon (Fig. 1H).
127 Incorporation of the TALEN-mediated deletion in the *dscaml1* mRNA was confirmed by RT-PCR and
128 sequencing. The deletion results in frame shift and a truncated open reading frame, which lacks the
129 signal peptide and all functional domains. These results suggest *dscaml1^{vt1}* is likely a null allele.

130 Homozygous mutant animals showed behavioral and morphological changes associated with the
131 visual system. At 5 dpf, homozygous mutant animals (*dscaml1*-/-) appeared to develop normally,
132 with normal head size, normal eye size, and inflated swim bladders. Compared with heterozygous
133 and wild-type siblings, however, mutant animals had darker pigmentation when placed on a light
134 background (Fig. 1I). This deficit in background adaptation, a camouflage response that requires
135 light detection, suggests that *dscaml1*-/- animals may be visually impaired²². At later stages,
136 lethality was observed in mutant animals at 8 dpf, and none survived past 11 dpf (Fig. 1J).
137 Heterozygous animals (*dscaml1*+/-) are viable and fertile as adults. Despite the late larval stage
138 lethality, *dscaml1* mutant brain showed no gross abnormalities. Major longitudinal and
139 commissural axon tracts, motor axon terminals, and peripheral ganglia are formed normally in
140 mutants (Supplementary Fig. S1). The only observed morphometric difference was in the optic
141 tectum neuropil region, a major retinorecipient area important for sensory processing. The optic
142 tectum neuropil was 23% larger in *dscaml1* mutants ($44,121 \pm 1,017 \mu\text{m}^2$) versus wild type
143 ($35,816 \pm 656.5 \mu\text{m}^2$) or heterozygotes ($36,715 \pm 549 \mu\text{m}^2$) ($p < 0.0001$, one-way ANOVA)
144 (Supplementary Fig. S1D).

145 ***dscaml1* is required for planar and laminar patterning in the retina**

146 Genetic studies in mice and chick demonstrated that Dscaml1 is required for planar patterning of
147 retinal amacrine cells and laminar specific neurite termination in the inner plexiform layer (IPL)⁶,
148^{20, 23}. We found that *dscaml1* has conserved functions in retinal patterning in zebrafish (Fig. 2). With

149 H&E staining, we did not see visible perturbation of retina structure, with the exception that the IPL
150 is thicker in the heterozygotes and mutants, compared to wild types (Fig 2A-B). Increased IPL
151 thickness was also seen in *Dscam* and *Dscaml1* mutant mice, and may be caused by decreased
152 developmental cell death^{20,23}. To test *dscaml1*'s role in planar patterning, we labeled the serotonin
153 (5-HT) expressing amacrine cells. 5-HT cells represent a single amacrine cell type (S1) that is
154 sparsely distributed in the retina, with very few contacts between cell bodies (Fig. 2C)²⁴. In *dscaml1*
155 mutants, however, frequent clustering of 5-HT amacrine cells was observed. We calculated the
156 probability of one cell being immediately adjacent to another, termed aggregation index (density
157 recovery profile analysis was not possible due to the sparsity of this cell type in the larvae).
158 Compared to wild-type animals, the aggregation index in mutants was significantly increased (Fig.
159 2D). The increased aggregation seen in the mutants was not due to an increase in the number of 5-
160 HT amacrine cells, which was not significantly different between wild-type, heterozygote, and
161 mutant animals (Fig. 2E).

162 We also found that loss of *dscaml1* impacted laminar specific neurite termination in the IPL,
163 specifically of the ON-bipolar cell axon terminals (visualized with anti-PKC α)²⁵. ON-bipolar cells
164 transduce electrical activity in response to light increments (e.g., lights turning on) and have
165 dendrites that extend toward the OPL (where they synapse with photoreceptor cells) and axons
166 that form three discrete layers in the inner half of the IPL (the ON sublamina) (Fig. 2F)²⁶. This
167 distribution was quantified by measuring the fluorescent intensity of PKC α immunolabeling across
168 the thickness of the IPL, as defined by SV2 immunolabeling²⁷. In all wild-type and heterozygote
169 animals, three distinct peaks at stereotypical positions can be discerned. In contrast, PKC α
170 distribution in the mutants was more diffuse and did not form three discrete sublaminae (Fig. 2G).
171 Cone photoreceptors and Müller glia appear morphologically normal in the *dscaml1* mutant retina
172 (Fig. 3A-F).

173 Loss of *dscaml1* did not appreciably affect the afferent projections of the retina. We utilized the
174 *Tg(atoh7:GAP-RFP)* transgenic line, which expresses membrane-tagged red fluorescent protein in
175 retinal ganglion cells²⁸. In *dscaml1* mutants, the optic nerve crossed the chiasm normally, and the
176 axon terminals (arborization fields) of the optic tract were mostly indistinguishable from wild-type

177 and heterozygous animals (Fig. 3G-I) ²⁹. This suggests that the expression of *dscaml1* in the GCL is
178 not required for outgrowth of retinal ganglion cell axons. It remains possible, however, that the
179 projections of a subset of retinal ganglion cells may be affected by the loss of *dscaml1*. Overall, the
180 expression and mutant phenotypes of zebrafish *dscaml1* demonstrate that it is functionally
181 conserved with other vertebrates and required for both planar and laminar patterning in the retina.

182 **Abnormal locomotor behavior in *dscaml1* mutants**

183 Given the retinal patterning deficits and background adaptation abnormality seen in the mutants,
184 we asked whether light-induced locomotor activity is also affected. We monitored locomotor
185 activity of individual 5 dpf larvae over 24 hours, under normal circadian cycle (14 h day/10 h night)
186 (Fig. 4A) ^{30,31}. Consistent with previous studies, wild-type fish were more active during the day, less
187 active at night, and responded robustly during day/night and night/day transitions ³⁰. This diurnal
188 rhythm was preserved in *dscaml1* mutants. Loss of *dscaml1* did not affect the duration of active
189 periods, during either day or night (Fig. 4B, C). The amount of movement, however, was reduced in
190 mutants during the day as well as the response to lights turning on, compared to wild-type and
191 heterozygous animals (Fig. 4D-F). Interestingly, the response in mutants to lights off was as robust
192 as for wild-type and heterozygous siblings (Fig. 4G). These results show that *dscaml1* mutants can
193 detect light and move in response to a light offset, but are deficient in responding to light onset.
194 These behavioral deficits are consistent with a partial deficit in the retinal ON pathway, potentially
195 contributed by imprecise sublamina-specific ON-bipolar cell axon targeting.

196 **Abnormal OKR and eye lock up in *dscaml1* mutants**

197 To further test the role of *dscaml1* in neural circuit function and sensorimotor integration, we
198 examined the mutants' performance in OKR. OKR consists of visual motion (*i.e.*, optic flow)-
199 triggered tracking eye movements (slow phases) and intervening resetting saccades (fast phases)
200 (Fig. 5A). The quality of OKR is measured by slow-phase gain, which is the ratio of eye velocity to
201 the velocity of the visual motion. In zebrafish, OKR develops early and is robust by 3-4 dpf ¹⁸. We
202 tested 5-6 dpf larvae inside a circular arena where black and white moving gratings were projected
203 onto the arena, and eye position was video-recorded simultaneously (Fig. 5A, Movie 1). Grating

204 directions alternated between clockwise and counter-clockwise at 3 or 40 seconds (Fig. 5B, E).
205 Under short time scale (3 s), fast phase has little effect on OKR performance, and gain is directly
206 related to the processing of optic flow via the vestibular premotor pathway (Fig. 1A) ^{32, 33}. Under
207 long time scale (40 s), saccades are necessary to reset eye position periodically, and the oculomotor
208 system needs to be robust against eye position drifts and fatigue in optic flow response ^{19, 34, 35, 36}.

209 We found that visuomotor processing for optic flow is intact in *dscaml1* mutants. Under short time
210 scale, both control (wild type and heterozygote) and mutant animals exhibited qualitatively normal
211 optokinetic responses (Fig. 5B-D). Slow-phase gain increased linearly with the logarithm of stimulus
212 contrast in both groups, and there was no difference in gain at lower contrast levels (contrast \leq 0.2)
213 (Fig. 5H). Mutants do have lower slow-phase gain than the controls at higher contrast levels
214 (contrast=0.5 or 1), though the deficit is mild. These findings suggest that *dscaml1* is likely not
215 required for the assembly or function of the vestibular premotor pathway, but affects OKR
216 performance at conditions that elicit higher eye velocity ³².

217 Under long time scale, *dscaml1* mutants showed deficits in saccadic eye movements and exhibited
218 more pronounced behavioral fatigue. In control animals, fast phase (resetting saccade) and slow
219 phase alternated regularly, and saccades had consistent frequency and amplitude (Fig. 5F). In
220 mutants, resetting saccades were irregular and reduced in amplitude (Fig. 5G, I). Interestingly,
221 mutant eye movements would frequently pause, similar to the “lock up” phenotype seen in human
222 with saccade deficits ¹⁶. Lock-up periods tended to occur towards the end of the stimulus period,
223 and the probability of lock up increased linearly over time, both in controls and mutants (Fig. 5J).
224 The probability of lock up (time bins where velocity $<1^{\circ}/s$) was significantly higher in mutants,
225 compared to controls (comparison of linear regression intercepts, $p<0.0001$) ^{35, 36}. Lock-up events
226 could occur throughout the eye position range in the mutants, suggesting that lock up is not due to
227 a failure to initiate faste phase at more eccentric positions (Supplementary Figure S2). Concurrently,
228 relative to controls, mutants had more pronounced decay of slow-phase gain over time, even when
229 lock-up periods were excluded (Fig. 5K, L) ^{19, 37}. In both control and mutant data sets, the decay of
230 slow-phase gain was well fit with a double exponential. Loss of *dscaml1* resulted in a drop in the
231 contribution by the longer (later) component, and faster decay in the shorter (earlier) component

232 (Table I., decay constant for short component shown in Fig. 5K, L). These results suggest that
233 *dscaml1* has important roles in saccade generation and velocity maintenance.

234 ***dscaml1* is required for torsional eye movements during VOR**

235 Our OKR assays tested the capacity for horizontal gaze stabilization, which requires the lateral and
236 medial recti. To test the functionality of the other four extraocular motoneuron populations, we
237 measured the gravito-inertial VOR in the torsional plane (Fig. 5M, N). In response to nose-up pitch
238 tilts, larvae will use their superior oblique and inferior rectus muscles to counter-rotate the eyes.
239 Similarly, following nose-down pitch tilts, larvae stabilize their gaze using the superior rectus and
240 inferior oblique muscles³⁸. As expected, wild-type larvae at 5dpf showed strong VOR in response to
241 15° steps up or down away from horizontal, with a slightly stronger response to nose-up tilts.
242 *dscaml1* mutants were able to initiate VOR in a directionally appropriate manner but had lower gain
243 (max eye velocity/max table velocity, 35°/s) to both stimuli. As fish develop VOR in the absence of
244 light, this deficit is likely not due to any visual impairment¹⁸. We conclude that *dscaml1* is involved
245 in the performance of both the OKR and VOR, and in both the horizontal and torsional planes.

246 ***dscaml1* is required for saccade and fixation**

247 Given the pronounced reduction in fast-phase response and faster decay of slow-phase response
248 during OKR, we next examined spontaneous eye movements in the absence of structured visual or
249 vestibular stimulus to assess specific deficits in saccade generation and neural integrator function.
250 Spontaneous eye movements in zebrafish consist of intermittent saccades, followed by periods of
251 fixation, similar to mammalian scanning saccades^{19, 34}. This behavior is used to direct visual
252 attention to the temporal retina, where photoreceptor density is highest^{39, 40}. Spontaneous saccades
253 are conjugated and usually alternate in direction, with typical angular velocity (sampled at 5 Hz)
254 greater than 100°/s (Fig. 6A). In control animals, spontaneous saccades with velocity greater than
255 100°/s were the predominant type of eye movement (59%) (Fig. 6C, D). In mutant animals, high-
256 velocity saccades were nearly absent (Fig. 6B-D). Instead of alternating in directions, sequential
257 saccades often moved in the same direction, suggesting that these eye movements may be short of

258 their intended target (hypometric). Saccades in mutants were also significantly more disconjugated,
259 indicating that saccade initiation was bilaterally desynchronized (Fig. 6B, E).

260 The reduced saccade velocity in mutants may reflect slower eye movements caused by dysfunction
261 in the oculomotor periphery. Alternatively, reduced saccade velocity may be coincidental to smaller
262 saccade amplitudes, which generally have lower velocity. We tested the correlation of peak velocity
263 and saccade amplitude, a linear relationship known as main sequence ^{19, 41}. Main sequence is a
264 clinically relevant diagnostic metric for saccade: patients with COMA have smaller saccade but
265 normal velocity (normal main sequence), whereas patients with saccade deficits associated with
266 neurodegenerative disorders have both smaller saccade and lower velocity (lower main sequence)
267 ^{17, 42}. We tested the spontaneous saccade main sequence (sampled at 30 Hz) and found that there
268 was no significant difference between mutants and controls ($p=0.468$, ANCOVA) (Fig. 6F). In other
269 words, saccades in *dscaml1* had smaller amplitude, but velocity was normal for the given amplitude.
270 The normal main sequence in mutants also suggests that the ocular periphery is not significantly
271 affected by the loss of *dscaml1*. Consistent with this finding, we did not see any gross abnormality
272 in the abducens motor neuron projection to the lateral rectus muscle in the mutants (Fig. 6G, H).

273 In addition to saccade deficits, post-saccade fixation was significantly perturbed in *dscaml1*
274 mutants, indicating a deficit in the neural integrator pathway. The integrator pathway provides
275 tonic activation of motor neurons to maintain fixation, counteracting spring forces in the eye plant
276 that would cause a drift back to the null position (arrows in Fig. 6A, B); during sustained OKR in a
277 given direction, this pathway is also necessary for converting tonic eye velocity commands to ramp-
278 like eye position commands. We modeled this drift rate using an exponential decay function and
279 found that eye position in mutant animals drifted towards baseline more rapidly than in controls
280 (median $\tau = 24$ and 7 seconds for control and mutant animals, respectively, Fig. 6I). Together, these
281 results suggest that *dscaml1* is involved in the function of the saccadic and integrator pathways, but
282 does not affect the function of the oculomotor periphery ⁴³.

283 **Loss of *dscaml1* leads to neural activity deficits during OKR fast phase**

284 To understand the neurophysiological basis of the oculomotor phenotypes, we focused on the
285 activity of the abducens motor complex (ABD), which controls the extraocular muscles for
286 horizontal eye movements and serves as the convergence point for different premotor inputs (Fig.
287 1A)^{44, 45}. We performed two-photon calcium imaging in control (*dscaml1+/-*) and mutant (*dscaml1-/-*)
288 fish in *elavl3:H2B-GCaMP6f* transgenic background while they performed OKR⁴⁶. Eye positions
289 were recorded simultaneously with an infrared video camera and oculomotor behavior-encoding
290 ABD neurons (motor or internuclear) were then identified based on anatomical location and
291 calcium activity (Fig. 7A-B)¹³. To induce a mixture of optokinetic and spontaneous responses we
292 projected a grating stimulus in front of the animal and then moved that stimulus in a repeating
293 temporal pattern (Fig. 7C-D). We measured mean fluorescence following the onset of stimulus
294 movement in either the ipsilateral (e.g., clockwise for right ABD) or contralateral (e.g.,
295 counterclockwise for right ABD) direction. Slow phase ABD activity (a proxy for vestibular pathway
296 activity) was calculated with deconvolved calcium signal for the first three seconds of the ipsilateral
297 or contralateral phases. Fast-phase ABD activity (a proxy for saccadic pathway activity) was
298 calculated with deconvolved average fluorescence following saccadic eye movements in both
299 directions. Since ABD neuron responses are direction selective, we could excite neurons in both
300 hemispheres by alternating the direction of stimulus movement.

301 Loss of *dscaml1* did not affect ABD activity during slow phase (n=86 cells from 3 control animals;
302 n=424 cells from 6 mutant animals). Population-average activity in the ABD was comparable in
303 mutant and control animals following the onset of stimulus movement in the ipsilateral direction
304 (Fig. 7E, F). In the contralateral direction, ABD population-average activity reached similar steady-
305 state levels in mutant and controls. This result is consistent with *dscaml1*'s relatively mild effect on
306 slow phase at short time scale and suggests that the vestibular pathway is unaffected.

307 In contrast, ABD activity was substantially reduced in mutants during fast phase, relative to
308 controls. The saccade-triggered average activity (STA) of ABD cells in the control animals were
309 characterized by a rapid increase or decrease in deconvolved fluorescence following an ipsilateral
310 or contralateral saccade, respectively (Fig. 7G, H). The STA of mutant ABD cells following fast-phase
311 events in either direction was reduced in both directions, compared to controls. Comparing the
312 distribution of trial-averaged STA amplitudes, *dscaml1* mutants had significantly lower amplitudes

313 than controls ($p < 0.05$, two-sample K-S test, $n=110$ cells from 3 control animals, $n=253$ cells from 7
314 mutant animals).

315 Together, our results show that oculomotor deficits originate centrally and that *dscaml1* affects ABD
316 response selectively during the fast phase. The population-level calcium response in ABD suggests
317 that mutant ABD neurons have normal ramping during the slow phase but lack the saccade-
318 associate burst activity seen in controls. These findings support the idea that *dscaml1* plays a
319 specific role in the function of the saccadic pathway.

320 Discussion

321 We investigated the cellular and behavioral roles of *dscaml1* in zebrafish and took advantage of the
322 oculomotor system to deduce *dscaml1*'s function within a defined neural circuit. Our results
323 underscore the importance of DSCAM proteins in retinal patterning and visuomotor function. Our
324 neurophysiological findings further showed that loss of *dscaml1* leads to impairment in the saccadic
325 but not the pretectum-vestibular premotor pathway, indicating a subcircuit requirement for
326 *dscaml1*. The collection of oculomotor deficits in *dscaml1* mutants bears a striking resemblance to
327 human COMA, for which no animal models exist.

328 *dscaml1 and retinal development*

329 Our results show that zebrafish *dscaml1*, like its mammalian ortholog, is required for maintaining
330 cellular spacing and refining neurites into discrete synaptic laminae in the retina. In the retina,
331 distinct cell types are organized in a mosaic pattern horizontally, and neurites stratify vertically in
332 precise layers in the inner and outer plexiform layers⁴⁷. Both aspects of spatial patterning require
333 the function of DSCAMs. We show that in zebrafish, loss of *dscaml1* causes serotonergic amacrine
334 cells to aggregate. In the IPL, axon terminals of PKC α -positive ON-bipolar cells are more diffuse in
335 *dscaml1* mutants, which likely affects laminar specific synaptogenesis. As ON-bipolar cell axon
336 maturation is activity independent, this diffuse terminal morphology reflects a delay or failure in
337 axon terminal development^{26, 27}. Interestingly, Dscam rather than Dscaml1 is involved in ON-
338 bipolar cell axon stratification in mice. Nevertheless, Dscaml1 is involved in the refinement of
339 neurite stratification in both mice (VGLUT3+ amacrine cells) and chicken (retinal ganglion cells)⁶.

340 23. These results demonstrate the remarkable functional conservation of *Dscaml1* across vertebrate
341 species.

342 How the retinal patterning deficits observed in *dscaml1* mutants affect visual function in *dscaml1*
343 still remains to be tested, but the collection of behavioral phenotypes provides some clues. The
344 reduced light-on locomotor response and darker pigmentation in *dscaml1* mutants are suggestive
345 of a reduction in ON pathway function. Consistent with this, the sluggish locomotor response to
346 light-on observed in the *dscaml1* mutant animals resembles the *no optokinetic response c* (*nrc*)
347 mutant, which completely lacks retinal ON-responses⁴⁸. The more diffuse targeting of ON-bipolar
348 cell axons in *dscaml1* mutants may lead to reduced strength or specificity of light-on responses.
349 However, in contrast to *nrc* animals, which cannot perform OKR, *dscaml1* animals can still perform
350 OKR. Therefore, it is most likely that ON-response is reduced but not completely abolished in
351 *dscaml1* mutants.

352 *Oculomotor behavior and neural circuit function*

353 The combination of behavioral assays and functional imaging showed that *dscaml1* was necessary
354 for the function of the oculomotor circuit. We focused our analysis to three subcircuits for horizontal
355 eye movements: the saccadic, vestibular, and integrator premotor pathways.

356 Loss of *dscaml1* strongly affected the saccadic pathway, as deficits were observed in mutants during
357 both reflexive saccades (OKR) and spontaneous scanning saccades. This is consistent with
358 physiological observations showing that saccade-related activity in the abducens was significantly
359 decreased in mutants compared to controls. Retinal defects may contribute to the saccade deficits
360 observed in mutants, at least during reflexive saccades, but would not account for the full extent of
361 the phenotype. Instead, our results favor the hypothesis that abnormal function of the saccadic
362 premotor pathway is the primary cause of the saccade phenotype in *dscaml1* mutants. It is
363 hypothesized that the saccade generator circuit relies on strong local recurrent feedback to
364 generate large and coordinated pulses⁴⁹. This feedback may be easily disrupted through the
365 expected connectivity deficits induced by *dscaml1* mutation. Another factor contributing to the
366 saccadic deficit could be attenuated connectivity at the EBN-ABD synapse. However, the

367 disconjugation of saccades observed in *dscaml1* mutants suggests that the pulse signal from the
368 saccade generators is already fragmented or weakened before being projected to the ABD.

369 We saw relatively mild deficits in the vestibular pathway. OKR slow phase performance at short
370 time scale was mostly normal in mutants, consistent with the normal ABD calcium dynamics during
371 slow phase. *dcaml1* mutant animal's performance dropped off at higher speeds, but the effects were
372 relatively mild. Given the essential role of the retinal ON pathway in OKR⁴⁸ and the diminished
373 behavioral responses to light onset (locomotor and background adaptation), the normal slow phase
374 performance may be due to compensatory mechanisms that overcome reduced retinal sensory
375 input. It is also worth noting that torsional VOR was affected more strongly than horizontal OKR,
376 indicating that *dscaml1*'s effect on different subcircuits of the oculomotor system is not uniform.

377 Loss of *dscaml1* resulted in a notable deficit in the function of the integrator pathway. This is most
378 clearly seen in the fast decay of eye fixation after spontaneous saccade in *dscaml1* mutants, relative
379 to controls. Additionally, slow phase deficits in mutants may partly arise from the integrator
380 pathway, which is necessary to integrate the velocity signal from the vestibular nuclei to encode a
381 smooth ramp of eye position⁵⁰. The behavioral dysfunction observed in the mutant could arise from
382 a deficit in the circuit connectivity within the integrator for supporting and coordinating persistent
383 firing^{45, 51}.

384 Lastly, the pronounced time-dependent fatigue and lock up phenotypes in *dscaml1* mutants are
385 likely contributed by a combination of different pathways and broader effects beyond the
386 oculomotor circuit. Decreased neurotransmitter release from optic nerve terminals and habituation
387 of retinorecipient neurons have previously been shown to degrade visual response under
388 prolonged stimulation; these mechanisms may underlie the reduced robustness in *dscaml1* mutants
389^{35, 36}. Similarly, lock up may result from changes in neuronal excitability and seizure-like episodes,
390 analogous to what was seen in the zebrafish *didy* mutants (see next section)³⁴.

391 *Comparison with didy (Nav1.1b) mutants*

392 Some aspects of the *dscaml1* phenotype are similar to a previously described zebrafish mutant, *didy*,
393 which encodes the voltage-gated sodium channel Scn1lab (Nav1.1b)³⁴. *didy* mutants have

394 spontaneous seizure-like brain activity and very infrequent spontaneous saccades. After 15 seconds
395 of continuous OKR stimulation, *didy* mutants cease to initiate resetting saccades, resulting in lock
396 up of the eyes. Another similarity between *didy* and *dscaml1* is defective light adaptation (darker
397 pigmentation, slow response to light stimulus). *didy* and *dscaml1* may both affect the saccadic
398 pathway, which progressively loses excitability in *didy* mutants. It is important to note, however,
399 that the saccade phenotypes are distinct between *didy* and *dscaml1*. In *didy* animals, saccades have
400 normal speed and amplitude³⁴, whereas saccades in *dscaml1* animals are slow and small.
401 Furthermore, lock-up events in *dscaml1* mutants occur more sporadically and across the position
402 range, whereas lock up only occurs at the most eccentric position at the end of a slow phase in *didy*
403 mutants. These distinctions suggest that *didy* and *dscaml1* likely affect saccade generation through
404 independent mechanisms

405 *Relevance to human oculomotor disorder*

406 *dscaml1* mutant fish share several features of COMA: failure to initiate saccadic eye movements,
407 hypometric saccades, normal main sequence, and intermittent lock up during horizontal OKR.
408 COMA is an infantile-onset condition involving failure of both voluntary and reflexive saccadic eye
409 movements^{16, 17, 52}. As it is not a true apraxia (where only voluntary movements are affected), the
410 condition is also known as intermittent saccade initiation failure or infantile-onset saccade
411 initiation delay. The etiology of COMA is still poorly understood. Genomic regions surrounding the
412 causative gene for juvenile nephronophthisis (*NPHP1*) have been suggested to contribute to COMA,
413 but mutations in *NPHP1* itself do not consistently cause COMA⁵³. *NPHP1* has been linked to primary
414 cilia function, which is crucial for the development of the cerebellum, a key region involved in
415 saccade control^{54, 55, 56}. Although there is currently no genetic association between human *DSCAML1*
416 and COMA (*DSCAML1* resides on a separate chromosome from *NPHP1*), further analysis of the
417 *dscaml1* mutants (e.g., cerebellum and extraocular motor neurons) may provide insights to the
418 pathogenesis of COMA and the development of neural circuitry for saccades in general.

419 *Conclusions*

420 Our investigations on zebrafish *dscaml1* revealed essential roles for a *DSCAM* family gene in
421 visuomotor behavior and subcircuit activity. Given the structural conservation of subcortical

422 circuits and the functional conservation of *dscaml1*'s roles in retinal patterning, it is plausible that
423 the mammalian *DSCAML1* will also contribute to visuomotor processing. By taking advantage of the
424 translucent larval zebrafish system, we recorded oculomotor circuit output dynamics in behaving
425 animals and uncovered a specific dependence of the saccade pathway on *dscaml1*. Our physiological
426 findings in both control and mutant contexts provide a neural basis for the saccade deficits seen in
427 *dscaml1* mutants and potentially for human saccade palsy (COMA). In addition to saccade deficits,
428 our broad examination of oculomotor behaviors also revealed *dscaml1*'s function in VOR, neural
429 integration, and behavioral robustness. These behavioral characterizations provide links between
430 *dscaml1* and diverse aspects of sensorimotor function and will facilitate future studies on the
431 development and disorders of sensorimotor circuits.

432

433 **Materials and Methods**

434 Zebrafish husbandry

435 Zebrafish (all ages) were raised under 14h light/10h dark cycle at 28.5°C. Embryos and larvae were
436 raised in water containing 0.1% Methylene Blue hydrate (Sigma-Aldrich). At 24 hours post-
437 fertilization, embryos used for histological analyses were transferred to E3 buffer containing
438 0.003% 1-phenyl-2-thiourea (PTU; Sigma-Aldrich) to prevent pigment formation. Developmental
439 stages are as described by Kimmel et al. ⁵⁷. All experimental procedures are performed in
440 accordance with Institutional Animal Care and Use Committee guidelines at Augusta University,
441 Virginia Tech, and Weill Cornell Medical College.

442 Mutant and Transgenic Zebrafish lines

443 *dscaml1* (ZFIN gene name: *Down syndrome cell adhesion molecule like 1*) mutant was generated in
444 TL/AB mixed background using TAL effector nucleases (TALENs) as previously described ^{21,58}. Two
445 alleles were identified, one harbored a 6 base pair insertion (in frame) and the other harbored a 7
446 base pair deletion (frame shift). The 7 base deletion mutant (*dscaml1^{vt1}*) was used for further
447 analysis. The *dscaml1^{vt1}* allele generates a HaeIII (New England Biolabs) restriction site, which was
448 used to distinguish between wild-type and *dscaml1^{vt1}* alleles. DNA prep and PCR were performed as

449 described previously⁵⁹, followed by HaeIII digestion for 2 hours at 37°C (primer sequences:
450 aaatactgcacggtgcacacgtc and atgcagatccatcagcctataatc). After HaeIII digestion, wild-type band was
451 395 base pairs (uncut) whereas mutant bands were 315 and 75 base pairs. Sequencing of *dscaml1*
452 transcript confirmed incorporation of the 7-base deletion into the open reading frame.
453 *Tg(atoh7:GAP-RFP)* animals were provided by Owen Randlett (Harvard University, Cambridge, MA,
454 USA)²⁸. *Tg(elavl3:H2B-GCaMP6f)* and *casper* (*nac*-/-; *roy*-/-) animals were provided by Misha Ahrens
455 (HHMI Janelia Farm Research Campus, Ashburn, VA, USA)⁴⁶.

456 Image acquisition and processing

457 Imaging procedures were as previously described⁶⁰. Fluorescent images were acquired using an
458 Olympus FV1000 laser-scanning confocal system with a 20x XLUMPlanFl water-immersion
459 objective or a Nikon A1R MP+ laser scanning confocal system with a CFI75 Apochromat LWD 25x
460 water-immersion objective. Larvae were immobilized with 0.01% tricaine methanesulfonate (MS-
461 222, Sigma-Aldrich), embedded in molten 1.5% low-melt agarose (Fisher Scientific) in a glass-
462 bottomed Petri dish (P50G-1.5-14-F, MatTek). Fish were mounted so that the surface to be imaged
463 was facing the glass bottom.

464 Images were processed with Fiji⁶¹ and Photoshop (Adobe Systems) software. To measure the extent
465 of serotonergic amacrine cell aggregation, we acquired confocal stacks and determined the center
466 of mass for each 5-HT positive cell in (x, y, z) coordinates. Intercellular distance between two cells
467 was calculated by the distance formula: $d = \sqrt{(x_2 - x_1)^2 + (y_2 - y_1)^2 + (z_2 - z_1)^2}$. For each cell,
468 intercellular distance to all other cells in the same retina were calculated. Cells with neighboring
469 cells within 3 cell diameter (≤ 10 microns) were categorized as aggregated. For each eye, the number
470 of aggregating cells was divided by the total number of cells to calculate aggregation ratio.

471 Quantification of the distribution of PKC α immunolabeling was performed as described by Nevin *et*
472 *al.*²⁷ Using Fiji, a rectangle was drawn across a relatively flat section of the IPL so that the top and
473 bottom of the rectangle abut the boundaries of the IPL, as defined by SV2 immunolabeling. Next, the
474 Plot Profile function was used to measure the average fluorescence intensity across the thickness
475 of the IPL. After exporting numerical data to Excel (Microsoft Inc.), data were normalized to maximal

476 fluorescence intensity and relative position within the IPL. The number of serotonergic neurons
477 were estimated by manually counting 5HT+ cells from 7 optical sections (10 μ m apart, at horizontal
478 levels adjacent to the lens) in each fish.

479 For 3D rendering of retinal afferents, *Tg(atoh7:GAP-RFP)* transgenic fish were fixed with 4% PFA
480 and mounted laterally. The eye on the imaged side was removed to allow visualization of the optic
481 tract. 3D rendering was created using Nikon NIS-Elements software. Measurements of images were
482 analyzed using the Prism 6 statistic software (GraphPad).

483 *Fluorescent in situ hybridization and immunohistochemistry*

484 *dscaml1* probe was generated by 5'RACE (Smart RACE cDNA Amplification Kit, Clonetech) using 3'
485 primers designed from Ensembl exon predictions. Amplified DNA was cloned into the pCRII-TOPO
486 vector by TA cloning (Invitrogen). Probe sequence includes 127 base pairs of 5' untranslated region
487 and 545 base pairs of coding sequence. DIG-labeled *dscaml1* probe synthesis and whole mount *in*
488 *situ* hybridization were performed as previously described ⁶⁰. For 3 and 5 days post-fertilization
489 (dpf) samples, Dextran sulfate (Sigma-Aldrich) and 4-iodophenol (Fluka) were added to the
490 hybridization and tyramide solution to increase signal intensity ⁶². Whole-mount
491 immunohistochemistry was performed as described by Randlett et al. ⁶³. Primary antibodies used
492 were: Znp-1 (anti-synaptotagmin2, Developmental Studies Hybridoma Bank), anti-acetylated-
493 tubulin (Sigma), anti-SV2 (Developmental Studies Hybridoma Bank), anti-HuC/D (Invitrogen), anti-
494 HNK-1 (zn-12, Developmental Studies Hybridoma Bank), anti-5-HT (Sigma), anti-PKC α (Santa Cruz
495 Biotechnologies), zpr-1 (Zebrafish International Resource Center), and anti-Blbp (Abcam). Alexa
496 fluor-conjugated secondary antibodies were used after primary antibody incubation.

497 *Locomotor assay*

498 Individual 5 dpf larvae were placed into each well of a 24-well tissue culture plate (Fisher Scientific)
499 and transferred into a Zebrabox imaging chamber (Viewpoint). Locomotor activity of each larva was
500 tracked over 24 hours, with white LED illumination turned off at 10 pm and on at 8 am. Total
501 displacement over time was integrated every 10 minutes, measured as previously described ³¹.

502 OKR and saccade assays

503 VisioTracker 302060 (New Behavior TSE) was used for OKR and saccade assays. Eye movements of
504 individual fish were recorded by an overhead CCD camera. Zebrafish larvae were placed in the
505 center of a 50mm glass bottom petri dish (MatTek) and immobilized in 1.5-2% low melting agarose
506 (Fisher Scientific) in E3 buffer. Agarose around the eye was removed to allow free eye movement.
507 The dish was then filled with E3. To test slow phase performance under short periodicity, the
508 direction of black and white grating switched every 3 seconds with grating velocity at $7.5^{\circ}/s$. Each
509 experimental run (trial) was 108 seconds long and included twelve 9-second phases at varying
510 contrast levels (0.99, 1.0, 0.5, 0.2, 0.1, 0.05, 0.02, 0.05, 0.1, 0.2, 0.5, 1.0). For each animal, 5-6 trials
511 were tested and OKR response typically initiated during the first three trials (initiation trials).
512 Contrast sensitivity was calculated using trials recorded after the initiation trials. To exclude the
513 effect of response latency and the initial ramping up of eye velocity at stimulus onset, the first 1
514 second of each 3-second half period was excluded from analysis³³. Spontaneous saccades and OKR
515 performance under long periodicity were tested using a trial that contains four phases: (1) uniform
516 illumination (1-160s), (2) square wave grating with direction switching every 40s, contrast=1,
517 spatial frequency=0.05 cycles/ $^{\circ}$, and velocity= $10^{\circ}/s$ (161-400s), (3) uniform illumination (401-
518 480s), (4) square wave grating with direction switching every 8s, contrast=1, spatial
519 frequency=0.05cycles/ $^{\circ}$, and velocity= $10^{\circ}/s$ (481-560s).

520 A saccadic event was defined as sample periods where the instantaneous absolute eye velocity is
521 greater than $50^{\circ}/s$. Slow-phase eye velocity was measured as the mean, saccade-removed,
522 instantaneous velocity averaged across time within 1-second bins. Instantaneous velocity was
523 measured as the difference in smoothed eye position divided by the sample period (200ms, 5 Hz).
524 Eye position was smoothed using a median filter (Matlab medfilt1) of 5 sample periods (1s). We
525 excluded sample periods that fell between 0.5 seconds before and 2 seconds after each saccade to
526 remove the effects of saccade filtering and post-saccade plant relaxation⁶⁴. To analyze lock-up
527 probability and saccade conjugacy we measured eye velocity independently for each eye since lock-
528 up could occur independently on a given eye. Lock up periods are defined as 1-second bins where
529 average velocity is $<1^{\circ}/s$. Lock up probability was defined as the average number of lock up periods
530 across trials and both eyes. We defined a disconjugacy index as the ratio of left and right

531 instantaneous eye velocity magnitude at each time bin where a saccadic event occurs. The index is
532 defined so that the larger saccade velocity is in the numerator which means the index is always
533 greater than or equal to 1. For all other plots, instantaneous velocity was averaged across both eyes
534 before binning.

535 To calculate the main sequence of saccade, eye positions were recorded at 30 Hz (33 ms sample
536 period). Saccade peak velocity and amplitude were measured as described by Chen et al.⁴¹ The main
537 sequence was calculated as the slope of the linear regression for peak velocity and amplitude, using
538 the Prism6 software (Graphpad) ¹⁹.

539 To measure the drift rate in eye position following spontaneous saccades during the uniform
540 illumination period of the stimulus, we used a quasi-Newton unconstrained optimization (Matlab
541 fminunc with Algorithm set to quasi-Newton) to minimize the squared error between eye position
542 and the function

543 $Ae^{-t/\tau} + E_0,$

544 with variable parameters A and τ . E_0 was fixed to the mean position for the eye being fit. The
545 algorithm was initialized with tau set to 10 seconds and A set to the first eye position value in the
546 sample. We excluded positions that occurred between 0-1 seconds after each saccade, to avoid
547 fitting post-saccadic relaxation related to plant mechanics. Since the duration of spontaneous
548 fixations was variable, the fixation window analyzed was variable with typical values between 5-20
549 seconds. We only analyzed exponential fits that passed the following goodness-of-fit criteria: sum-
550 of-squared errors was less than $(30^\circ)^2$ or one minus the ratio of mean squared-error to the sample
551 variance was greater than 0.4 and the sum-of-squared errors was less than $(200^\circ)^2$. These criteria
552 were chosen based on visual inspection of fit qualities.

553 VOR assay

554 Torsional eye movements were measured in 5 days post-fertilization fish in response to step tilts
555 delivered using an apparatus similar in design to Schoppik *et al.* 2017 ³⁸. All experiments took place
556 in the dark. Larval fish were immobilized completely in 2% low-melting-temperature agar (Thermo

557 Fisher), and the left eye freed. The agar was then pinned (0.1mm stainless minutien pins, FST) to a
558 ~5mm² piece of Sylgard 184 (Dow Corning) which was itself pinned to Sylgard 184 at the bottom
559 of a 10 mm² optical glass cuvette (Azzota). The cuvette was filled with 1ml of E3 media and placed
560 in a custom holder on a 5-axis (X, Y, Z, pitch, roll) manipulator (ThorLabs MT3 and GN2). The fish
561 was aligned with the optical axes of two orthogonally placed cameras such that both the left utricle
562 and two eyes were level with the horizon (front camera). The experimenter running behavior was
563 blind as to the genotype of the fish.

564 The eye-monitoring camera (Guppy Pro 2 F-031, Allied Vision Technologies) used a 5x objective
565 (Olympus MPLN, 0.1 NA) and custom image-forming optics to create a 100x100 pixel image of the
566 left eye of the fish (6μm/pixel), acquired at 200Hz. The image was processed on-line by custom
567 pattern matching software to derive an estimate of torsional angle (LabView, National Instruments),
568 and data were analyzed using custom MATLAB scripts. A stepper motor (Oriental Motors AR98MA-
569 N5-3) was used to rotate the platform holding the cameras and fish. The platform velocity and
570 acceleration were measured using integrated circuits (IDG500, Invensense and ADXL335, Analog
571 Devices) mounted together on a breakout board (Sparkfun SEN-09268). Fish were rotated stepwise
572 for 4 cycles: from 0° to -15°, where positive values are nose-down, then from -15° to 0°, from 0° to
573 15°, then back to 0°. Steps had a peak velocity at 35°/sec. The inter-step interval was 7.5 seconds.

574 The eye's response across the experiment was first centered to remove any offset introduced by the
575 pattern-matching algorithm. Data were then interpolated with a cubic spline interpolation to
576 correct for occasional transient slowdowns (i.e., missed frames) introduced by the pattern-
577 matching algorithm. The eye's velocity was estimated by differentiating the position trace; high-
578 frequency noise was minimized using a 4-pole low-pass Butterworth filter (cutoff = 3Hz). Each step
579 response was evaluated manually; trials with rapid deviations in eye position indicative of
580 horizontal saccades or gross failure of the pattern-matching algorithm were excluded from analysis.
581 Across all fish and all steps used to measure the behavior, the median number of usable responses
582 was 7/10. The response to each step for a given fish was defined as the mean across all responses
583 to that step across cycles. The gain was estimated by measuring the peak eye velocity occurring over
584 the period 375-1000ms after the start of the step. Only steps away from the horizon were analyzed.

585 Of 9 fish, one was excluded because it had fewer than ten steps for analysis, all others had at least
586 ten. The median number of steps \pm interquartile range was $18/15 \pm 13.75/10.5$ for nose-down/nose-
587 up steps respectively.

588 *Two-Photon Calcium Imaging during Behavior*

589 Embryos from crosses of *dscaml1* heterozygous mutants, (*dscaml1+/-;casper+/-* X *dscaml1+/-*
590 *;nac+/-;elavl3:H2B-GCaMP6f*) were used. At 5-7 dpf, pigmentless (*nac-/-*) *dscaml1* heterozygous and
591 homozygous mutant siblings were immobilized in a gel of 1.8% low-melting temperature agarose
592 (Sigma-Aldrich) in preparation for imaging. Agarose was removed from the eyes to allow them to
593 move freely during imaging. Each fish was genotyped following imaging. Simultaneous eye tracking
594 and two-photon calcium imaging were performed using a custom-built system as previously
595 described¹³. Each image was acquired by raster scanning a mode-locked excitation laser
596 (wavelength set to 930 nanometers) through a 40x water immersion lens to a horizontal plane at
597 the abducens motor neurons. The laser power at the sample varied between 15-25 mW. For each
598 animal, we recorded 3-10 planes at a rate of 1.95Hz and duration of 5 minutes per plane. Each plane
599 was recorded while vertical stripes were projected onto a screen of diffusion film placed 1-3 cm in
600 front of the animal providing an optokinetic stimulus¹³. The stripes moved at a constant velocity
601 whose magnitude and direction changed in a repeating pattern that consisted of equal durations of
602 positive, negative, and zero velocity, with each phase lasting 3.14 (2 heterozygotes and 6 mutants)
603 or 31.26 seconds (1 heterozygotes and 1 mutant). Eye position was measured using a sub-stage,
604 infrared camera (Allied Vision Technologies, Guppy FireWire camera) that acquired frames at 13
605 Hz¹³.

606 *Identification of putative abducens neurons*

607 Putative abducens neurons were identified based on cell location and fluorescence activity.
608 Abducens motor neurons are clustered in rhombomeres (rh) 5-6 and are arranged in dorsal-ventral
609 columns. The imaging window ($185 \mu\text{m}^2$) was positioned over rh 5-6 using the posterior otolith as
610 guides to image the abducens population⁶⁵. We only examined cells whose fluorescence responses
611 were correlated with direction-rectified eye-position and/or eye-velocity traces with an absolute

612 Pearson correlation coefficient greater than or equal to 0.3^{13, 44, 51}. Before correlation calculation,
613 we convolved eye-position and eye-velocity variables with a 2 second exponentially decaying
614 calcium impulse response function to account for the calcium buffering associated with a cell's
615 action potential^{44, 66}. Single neurons that contained at least one pixel with an absolute correlation
616 value above 0.3 were manually selected for further analysis. To correct for animal motion artifacts,
617 fluorescence movies were first pre-processed using a procedure that relies on cross-correlation of
618 individual frames with a time-averaged reference frame⁵¹. Frames that undergo large shifts from
619 the reference frame (greater than the median plus 5 times the median absolute deviation) were
620 excluded from analysis. To compute delta F over F time series (dF/F), we subtracted and then
621 divided the time-averaged fluorescence within each ROI.

622 *Saccade and Stimulus-Triggered Average Calculation*

623 For each cell, we computed the average dF/F response relative to saccadic (fast-phase) eye
624 movements and relative to the start of optokinetic stimulus movements. A fast-phase event is
625 defined as described above (50 °/s). Eye velocity is computed as the instantaneous difference in
626 smoothed eye position divided by instantaneous eye sampling time (77 ms). Eye position was
627 smoothed using a median filter (Matlab medfilt1) of order equivalent to 500 ms. In order to combine
628 dF/F traces across saccadic events and the start of stimuli, we linearly interpolated saccade or
629 stimulus-aligned responses to a grid of evenly spaced time bins 333 ms in width before averaging.
630 We excluded planes from analysis if there are less than 5 saccades events available for computing
631 the STA. When averaging stimulus-aligned responses we only used traces where a fast-phase event
632 did not occur within the first 3 seconds following stimulus onset (n=3 hets, n=6 mutants).

633

634 **Acknowledgments**

635 This work was supported by funding from the National Institutes of Health (R01 EY024844 to Y.A.P.,
636 K99 EY027017 to A.D.R., R01 EY027036 to E.R.F.A.), the Medical College of Georgia, and Virginia
637 Tech. We thank the animal care staff at Augusta University and Virginia Tech for animal husbandry,
638 the Augusta University Electron Microscopy and Histology Core for retina histology preparation, A.

639 Pauli for help generating the *dscaml1* TALEN mutants, J. Mathias for assistance with locomotor
640 behavior analysis, F. Ali for technical assistance, and K. Bollinger and J. Sanes for helpful discussions.

641 **Author Contributions**

642 T.W., M.M., and Y.A.P. conceived the study, with input from A.F.S. Y.A.P., J.A.G. and S.Z. generated the
643 *dscaml1* mutant line, using TALEN targeting constructs designed and made by D.R., S.Q.T., and J.K.J.
644 T.W., M.M., R.R., C.K., and Y.A.P. contributed to the histological analyses. M.M., A.R. A.S., K.E.H., D.S.,
645 E.R.F.A. and Y.A.P. contributed to the behavioral analyses. A.R. and E.R.F.A. designed and interpreted
646 the functional imaging experiments. A.R. performed and analyzed the functional imaging
647 experiments with help from M.M. Y.A.P. wrote the manuscript, with contributions from T.W., M.M.,
648 A.R., R.R., D.S., S.L.G., and E.R.F.A.

649 **Figures and Movie**

650 **Movie 1. OKR response.** Control (left) and *dscaml1*-/- (right) animals performing OKR.

651 **Figure 1. The Oculomotor circuit, and the expression and gene targeting of *dscaml1*. A,**
652 Diagram of the oculomotor circuit for horizontal eye movement. Visual motion activates directional
653 selective retinal ganglion cells, which innervate the optic tectum (OT) and pretectum (PT). PT
654 provides input to the vestibular nucleus (VN). OT (along with other areas), activates the excitatory
655 burst neurons (EBN). EBN and VN provide premotor input to the abducens nucleus (ABD), which
656 innervates the extraocular muscles. EBN and VN also innervate the velocity-position neural
657 integrator (NI), which provides an eye position signal to the ABD. The saccadic, vestibular, and
658 integrator pathways are labeled light brown, dark brown, and blue, respectively. **B-G**, *dscaml1*
659 mRNA (white) labeled by fluorescent *in situ* hybridization, with neuropil counterstained with an
660 antibody against synaptotagmin 2 (Znp-1, magenta). Developmental staging as indicated. **H**,
661 Alignment of wild-type and TALEN targeted *dscaml1* genomic sequence. The start codon is boxed,
662 and the region containing insertions and deletions is highlighted in red. **I**, Pigmentation pattern of
663 different genotypes. *dscaml1* mutant animals show darker overall pigmentation. **J**, Survival curve,
664 sorted by genotype. GCL: ganglion cell layer; INL: inner nuclear layer; ONL: outer nuclear layer. Scale
665 bar is 100 μ m in panel A-F, 1mm in H.

666 **Figure 2. *dscaml1* is required for planar and laminar patterning of the retina. A**, H&E staining
667 of 5 dpf retina. **B**, Quantification of IPL thickness, performed in confocal imaged 5 dpf larvae
668 immunostained with Znp-1 antibody. Mutants have significantly thicker IPL compared to wild-type
669 animals. Heterozygotes have an intermediate phenotype. **C**, Serotonergic amacrine cells, stained
670 with an antibody against 5-hydroxytryptamine (5-HT). Cell bodies are indicated by yellow
671 arrowheads. **D**, Percentage of cells that are immediately adjacent to another cell (within 10 μ m,
672 approximately 3 cell diameter) is significantly higher in *dscaml1*-/- animals (**p<0.01, one-way
673 ANOVA). **E**, The number of 5-HT positive amacrine cells was not significantly different. **F**,
674 Immunostaining of ON-bipolar cell (PKC α , green), retinal ganglion cell [*Tg(atoh7:GAP-RFP)*, red],
675 and synapses (SV2, blue). Boxed areas are enlarged two-fold and shown in the inset. Both mutants
676 and morphants show loss of discrete stratification and mature terminal boutons in the ON (lower)
677 sublamina of the IPL. **G**, PKC α immunolabeling intensity (vertical axis) was plotted across the depth
678 of the IPL (horizontal axis), normalized for maximal intensity and IPL thickness. Three prominent
679 peaks can be discerned in wild-type and heterozygote animals (red arrowheads). The number and
680 location of peaks are more variable in mutants and morphants. GCL: ganglion cell layer; INL: inner
681 nuclear layer; IPL: inner plexiform layer; ONL: outer nuclear layer; OPL: outer plexiform layer. Scale
682 bars are 25 μ m. One-way ANOVA was used for statistical comparisons in D and E (****p<0.0001,
683 ***p<0.001, **p<0.01).

684 **Figure 3. Normal development of Müller glia, outer retina, and optic tract in the *dscaml1***
685 **mutant. A-F**, No abnormalities were seen in cone photoreceptor cells (stained with zpr-1 antibody)
686 and Müller glia (anti-Blbp). **G-I**, Retinal afferent projection in *dscaml1* mutants. The panel above G
687 shows an illustration of retinal afferents (red) in the *Tg(atoh7:GAP-RFP)* transgenic. Images show
688 the 3D reconstruction of retinal afferents viewed from the side (left images) and front (right
689 images). Retinal arborization fields (AFs) in the thalamus (AF4), pretectum (AF7, 9), and optic
690 tectum (AF10) are identified as described previously²⁹. No differences were observed among
691 different genotypes. OT: optic tract. Panels A-F are shown at the same scale, scale bar in A is 25 μ m.
692 Panels G-I are shown at the same scale, scale bar in G is 100 μ m.

693 **Figure 4. Locomotor activity in response to light.** **A**, Locomotor activity over 24 hours. Solid lines
694 are mean movement (n=8 for each group), and dotted lines indicate the range of standard error.
695 Lighting conditions are indicated on the X-axis, with each tick marking one hour. **B-C**, Percentage
696 time active during the day (B) and night (C). **D-E**, Average movement during the day (D) and night
697 (E). **F-G**, Total amount of movement 30 minutes after lights switch on (F) and off (G). *p<0.05 for
698 pairwise comparisons using one-way ANOVA.

699 **Figure 5. OKR and VOR performance in *dscaml1* mutants.** **A**, larvae were immobilized in the
700 center of a circular arena, where black and white vertical bars are projected. Diagram of eye position
701 is shown on the right, with fast phases (red segments) and slow phases (blue segments). **B-E**, short
702 time-scale OKR. Eye position traces are shown for control (C) and *dscaml1*-/- (D) animals, at the
703 same time scale as the square wave stimulus (B). Right and left eye traces are in black and fuchsia,
704 respectively. **E-G**, long time-scale OKR. Eye velocity and position traces are shown for control (C)
705 and *dscaml1*-/- (D), at the same time scale as the stimulus (E). In mutants, the eyes intermittently
706 became locked up (red arrowheads). **H**, slow-phase velocity across a range of contrast levels.
707 (*p<0.05, two-way ANOVA with Bonferroni correction). **I**, saccade amplitude is lower in mutants
708 (****p<0.0001, two-sample t-test). **J-K**, the temporal dependency of lock-up probability (J), slow-
709 phase gain (K), and slow-phase gain excluding lock-up periods (L). Positive gains in H, J-K are
710 defined as eye movement in the same direction as the stimulus. Regression lines, means, and
711 standard error (shaded areas) are shown. Linear regression model was used in J and control group
712 in K. Two phase exponential decay regression model with plateau constrained to zero was used for
713 *dscaml1*-/- group in K and both groups in L. **M**, eye velocity in response to a 35°/s tilt stimulus (black
714 dotted line) in wild-type (top panel, solid black line) and *dscaml1* mutant (bottom panel, solid red
715 line). Shaded areas indicate interquartile range. Torsional velocity was slower in mutants,
716 compared to wild type. **N**, velocity gain of upward and downward tilts, both of which are lower in
717 mutants. Mean values are marked by open circles. *p<0.05, Mann-Whitney U test.

718 **Figure 6. Spontaneous saccade and fixation are abnormal in *dscaml1* mutants.** **A-B**,
719 spontaneous saccades in control (A) and *dscaml1*-/- (B) were recorded during uniform illumination
720 (no gratings). Right and left eye traces are in black and fuchsia, respectively. Red arrowheads
721 indicate disconjugated saccades. **C**, the frequency of eye movements divided into angular velocity

722 bins. Controls had significantly more eye movements greater than 100°/s compared to mutants,
723 whereas mutants had more eye movements in the slowest bin compared to control (*p<0.05,
724 ****p<0.0001, two-way ANOVA). **D**, the relative frequency distribution of eye movements based on
725 angular velocity. Control animals perform significantly more fast eye movements than mutants
726 (p<0.0001, two-sample K-S test). **E**, cumulative distribution of saccade disconjugacy index for
727 controls and mutants (higher equals more disconjugated, see methods). Control index has a median
728 value of 1.56 across the population while the mutant index has a higher median value of 2.33.
729 Distribution is significantly different between control and mutant (p<0.001, two-sample K-S test).
730 **F**, peak velocity and amplitude for each saccade event was plotted, along with linear regression
731 (solid line). The slope is not significantly different between control and mutant (p=0.46). **G-H**, an
732 example of TagRFP-T expressing abducens motor neurons [from *Tg(mnx1:TagRFP-T)*] in wild-type
733 (G) and mutant (H) animal. Dorsal view, rostral to the left. Labeled structures: motor axons (VIth
734 nerve, white arrows), rostral abducens complex (green arrowheads), and caudal abducens complex
735 (magenta arrowheads). Scale bar is 100 μ m. **I**, eye position decay (arrows in A, B) calculated as $1/\tau$.
736 ****: p<0.0001, Mann-Whitney *U* test.

737 **Figure 7. Two-photon calcium imaging in Abducens and Inferior Olive neural populations. A-**
738 **D**, two-photon calcium imaging and simultaneous eye position recording during OKR. Circles in
739 time-averaged images show the locations of cells (A, B) with corresponding indices whose
740 fluorescence activity is shown (C, D). Circles in the abducens motor complex (ABD) are marked. **E**,
741 average fluorescence traces of individual cells (Y-axis) aligned to stimulus onset during slow-phase
742 activity (X-axis) in the ABD. **F**, Population average of fluorescence traces in E. **G**, average
743 fluorescence traces aligned to fast-phase eye movements for cells in the ABD. **H**, activity in G
744 averaged across the population. Error bars in F and H show the median absolute deviation of single-
745 cell activities from the population average divided by the square root of the number of cells,
746 normalized so that population responses are between -1 and 1.

747 **Supplementary Figure S1. Brain morphogenesis is grossly normal in *dscaml1* mutants. A-B**,
748 Lateral view of axon tracts (Ac-tub, green) and synapses (znp-1, magenta) at 1 and 5 dpf. In 1 dpf
749 embryos (A), no differences were seen in the formation of the major commissures and longitudinal

750 tracts⁶⁷. In 5 dpf larvae, no apparent abnormalities were seen in the morphology of sensory nerves,
751 motor nerves, or distribution of synapses in the brain and retina^{68, 69}. **C**, Lateral view of the
752 neuromuscular junction of the trunk, stained with a marker for presynaptic terminals (SV2). **D**,
753 Dorsal view of 5 dpf larvae stained for mature neurons (Hu, magenta) and axon tracts (HNK-1,
754 green). Areas outlined in yellow are the optic tectum neuropil region. Images show maximal
755 intensity projection of confocal image stacks. Scale bars are 100 μ m.

756 **Supplementary Figure S2. Eye Position during lock-up in *dscaml1* mutants.** Histogram of left
757 and right eye positions averaged during 1 second bins where lock-up occurs. Bin size is 2 degrees.

758 **Tables**

759 **Table I. Double exponential decay fit for slow phase gain.**

760

761 **References**

- 762 1. Iossifov I, *et al*. The contribution of de novo coding mutations to autism spectrum disorder.
763 *Nature* **515**, 216-221 (2014).
- 764 2. Karaca E, *et al*. Genes that Affect Brain Structure and Function Identified by Rare Variant
765 Analyses of Mendelian Neurologic Disease. *Neuron* **88**, 499-513 (2015).
- 766 3. Blank M, *et al*. The Down syndrome critical region regulates retinogeniculate refinement. *J
767 Neurosci* **31**, 5764-5776 (2011).
- 768 4. Cui S, Lao L, Duan J, Jin G, Hou X. Tyrosine phosphorylation is essential for DSCAML1 to
769 promote dendrite arborization of mouse cortical neurons. *Neurosci Lett* **555**, 193-197
770 (2013).
- 771 5. Maynard KR, Stein E. DSCAM contributes to dendrite arborization and spine formation in
772 the developing cerebral cortex. *J Neurosci* **32**, 16637-16650 (2012).
- 773 6. Yamagata M, Sanes JR. Dscam and Sidekick proteins direct lamina-specific synaptic
774 connections in vertebrate retina. *Nature* **451**, 465-469 (2008).

780

781 7. Zhang L, Huang Y, Chen JY, Ding YQ, Song NN. DSCAM and DSCAML1 regulate the radial
782 migration and callosal projection in developing cerebral cortex. *Brain Res* **1594**, 61-70
783 (2015).

784 8. Bruce FM, Brown S, Smith JN, Fuerst PG, Erskine L. DSCAM promotes axon fasciculation and
785 growth in the developing optic pathway. *Proceedings of the National Academy of Sciences of*
786 *the United States of America* **114**, 1702-1707 (2017).

787 9. Leigh RJ, Zee DS. *The neurology of eye movements*, 5th edition. edn. Oxford University Press
788 (2015).

789 10. Bittencourt J, *et al*. Saccadic eye movement applications for psychiatric disorders.
790 *Neuropsychiatr Dis Treat* **9**, 1393-1409 (2013).

791 11. Anderson TJ, MacAskill MR. Eye movements in patients with neurodegenerative disorders.
792 *Nature Reviews Neurology* **9**, 74 (2013).

793 12. Galicia CA, Sukeena JM, Stenkamp DL, Fuerst PG. Expression patterns of dscam and sdk
794 gene paralogs in developing zebrafish retina. *Molecular vision* **24**, 443-458 (2018).

795 13. Daie K, Goldman MS, Aksay ER. Spatial patterns of persistent neural activity vary with the
796 behavioral context of short-term memory. *Neuron* **85**, 847-860 (2015).

797 14. Straka H, Beck JC, Pastor AM, Baker R. Morphology and physiology of the cerebellar
798 vestibulolateral lobe pathways linked to oculomotor function in the goldfish. *J Neurophysiol*
799 **96**, 1963-1980 (2006).

800 15. Masseck OA, Hoffmann KP. Comparative neurobiology of the optokinetic reflex. *Ann N Y*
801 *Acad Sci* **1164**, 430-439 (2009).

802 16. Harris CM, Shawkat F, Russell-Eggitt I, Wilson J, Taylor D. Intermittent horizontal saccade
803 failure ('ocular motor apraxia') in children. *Br J Ophthalmol* **80**, 151-158 (1996).

804 17. Zee DS, Yee RD, Singer HS. Congenital ocular motor apraxia. *Brain* **100**, 581-599 (1977).

805 18. Easter SS, Jr., Nicola GN. The development of eye movements in the zebrafish (*Danio rerio*).
806 *Dev Psychobiol* **31**, 267-276 (1997).

807 818

819 19. Beck JC, Gilland E, Tank DW, Baker R. Quantifying the ontogeny of optokinetic and
820 vestibuloocular behaviors in zebrafish, medaka, and goldfish. *J Neurophysiol* **92**, 3546-3561
821 (2004).

822 20. Fuerst PG, *et al.* DSCAM and DSCAML1 function in self-avoidance in multiple cell types in
823 the developing mouse retina. *Neuron* **64**, 484-497 (2009).

825 21. Reyon D, Tsai SQ, Khayter C, Foden JA, Sander JD, Joung JK. FLASH assembly of TALENs for
826 high-throughput genome editing. *Nat Biotechnol* **30**, 460-465 (2012).

828 22. Wagle M, Mathur P, Guo S. Corticotropin-releasing factor critical for zebrafish camouflage
829 behavior is regulated by light and sensitive to ethanol. *J Neurosci* **31**, 214-224 (2011).

831 23. Garrett AM, Tadenev AL, Hammond YT, Fuerst PG, Burgess RW. Replacing the PDZ-
832 interacting C-termini of DSCAM and DSCAML1 with epitope tags causes different
833 phenotypic severity in different cell populations. *eLife* **5**, (2016).

835 24. Maurer CM, Schonthaler HB, Mueller KP, Neuhauss SC. Distinct retinal deficits in a zebrafish
836 pyruvate dehydrogenase-deficient mutant. *J Neurosci* **30**, 11962-11972 (2010).

838 25. Wan L, Almers W, Chen W. Two ribeye genes in teleosts: the role of Ribeye in ribbon
839 formation and bipolar cell development. *J Neurosci* **25**, 941-949 (2005).

841 26. Schroeter EH, Wong RO, Gregg RG. In vivo development of retinal ON-bipolar cell axonal
842 terminals visualized in nyx::MYFP transgenic zebrafish. *Vis Neurosci* **23**, 833-843 (2006).

844 27. Nevin LM, Taylor MR, Baier H. Hardwiring of fine synaptic layers in the zebrafish visual
845 pathway. *Neural Dev* **3**, 36 (2008).

847 28. Zollessi FR, Poggi L, Wilkinson CJ, Chien CB, Harris WA. Polarization and orientation of
848 retinal ganglion cells in vivo. *Neural Dev* **1**, 2 (2006).

850 29. Robles E, Laurell E, Baier H. The retinal projectome reveals brain-area-specific visual
851 representations generated by ganglion cell diversity. *Curr Biol* **24**, 2085-2096 (2014).

853 30. Prober DA, Rihel J, Onah AA, Sung RJ, Schier AF. Hypocretin/orexin overexpression induces
854 an insomnia-like phenotype in zebrafish. *J Neurosci* **26**, 13400-13410 (2006).

857 31. Farrell TC, Cario CL, Milanese C, Vogt A, Jeong JH, Burton EA. Evaluation of spontaneous
858 propulsive movement as a screening tool to detect rescue of Parkinsonism phenotypes in
859 zebrafish models. *Neurobiol Dis* **44**, 9-18 (2011).

860 32. Kubo F, Hablitzel B, Dal Maschio M, Driever W, Baier H, Arrenberg AB. Functional
861 architecture of an optic flow-responsive area that drives horizontal eye movements in
862 zebrafish. *Neuron* **81**, 1344-1359 (2014).

863 33. Rinner O, Rick JM, Neuhauss SC. Contrast sensitivity, spatial and temporal tuning of the
864 larval zebrafish optokinetic response. *Invest Ophthalmol Vis Sci* **46**, 137-142 (2005).

865 34. Schoonheim PJ, Arrenberg AB, Del Bene F, Baier H. Optogenetic localization and genetic
866 perturbation of saccade-generating neurons in zebrafish. *J Neurosci* **30**, 7111-7120 (2010).

867 35. Smear MC, *et al.* Vesicular glutamate transport at a central synapse limits the acuity of
868 visual perception in zebrafish. *Neuron* **53**, 65-77 (2007).

869 36. Perez-Schuster V, *et al.* Sustained Rhythmic Brain Activity Underlies Visual Motion
870 Perception in Zebrafish. *Cell Rep* **17**, 1098-1112 (2016).

871 37. Chen CC, *et al.* Velocity storage mechanism in zebrafish larvae. *The Journal of Physiology*
872 **592**, 203-214 (2014).

873 38. Schoppik D, *et al.* Gaze-stabilizing central vestibular neurons project asymmetrically to
874 extraocular motoneuron pools. *The Journal of Neuroscience*, (2017).

875 39. Bianco I, Kampff A, Engert F. Prey Capture Behavior Evoked by Simple Visual Stimuli in
876 Larval Zebrafish. *Frontiers in Systems Neuroscience* **5**, (2011).

877 40. Schmitt EA, Dowling JE. Early retinal development in the zebrafish, *Danio rerio*: light and
878 electron microscopic analyses. *J Comp Neurol* **404**, 515-536 (1999).

879 41. Chen CC, Bockisch CJ, Straumann D, Huang MY. Saccadic and Postsaccadic Disconjugacy in
880 Zebrafish Larvae Suggests Independent Eye Movement Control. *Front Syst Neurosci* **10**, 80
881 (2016).

882 42. Garbutt S, Harwood MR, Harris CM. Comparison of the main sequence of reflexive saccades
883 and the quick phases of optokinetic nystagmus. *Br J Ophthalmol* **85**, 1477-1483 (2001).

884

885

886

887

888

889

890

891

892

893

894

895

896 43. Sparks DL. The brainstem control of saccadic eye movements. *Nature reviews Neuroscience*
897 3, 952-964 (2002).

898 44. Miri A, Daie K, Burdine RD, Aksay E, Tank DW. Regression-based identification of behavior-
899 encoding neurons during large-scale optical imaging of neural activity at cellular
900 resolution. *J Neurophysiol* **105**, 964-980 (2011).

902 45. Vishwanathan A, Daie K, Ramirez AD, Lichtman JW, Aksay ERF, Seung HS. Electron
903 Microscopic Reconstruction of Functionally Identified Cells in a Neural Integrator. *Curr Biol*
904 **27**, 2137-2147 e2133 (2017).

906 46. Vladimirov N, *et al.* Light-sheet functional imaging in fictively behaving zebrafish. *Nat
907 Methods* **11**, 883-884 (2014).

909 47. Hoon M, Okawa H, Della Santina L, Wong RO. Functional architecture of the retina:
910 development and disease. *Progress in retinal and eye research* **42**, 44-84 (2014).

912 48. Emran F, Rihel J, Adolph AR, Wong KY, Kraves S, Dowling JE. OFF ganglion cells cannot
913 drive the optokinetic reflex in zebrafish. *Proceedings of the National Academy of Sciences of
914 the United States of America* **104**, 19126-19131 (2007).

916 49. Lo CC, Wang XJ. Cortico-basal ganglia circuit mechanism for a decision threshold in reaction
917 time tasks. *Nat Neurosci* **9**, 956-963 (2006).

919 50. Cannon SC, Robinson DA. Loss of the neural integrator of the oculomotor system from brain
920 stem lesions in monkey. *J Neurophysiol* **57**, 1383-1409 (1987).

922 51. Lee MM, Arrenberg AB, Aksay ER. A structural and genotypic scaffold underlying temporal
923 integration. *J Neurosci* **35**, 7903-7920 (2015).

925 52. Salman MS. Infantile-onset saccade initiation delay (congenital ocular motor apraxia). *Curr
926 Neurol Neurosci Rep* **15**, 24 (2015).

928 53. Betz R, *et al.* Children with ocular motor apraxia type Cogan carry deletions in the gene
929 (NPHP1) for juvenile nephronophthisis. *J Pediatr* **136**, 828-831 (2000).

931 54. Jauregui AR, Nguyen KCQ, Hall DH, Barr MM. The *Caenorhabditis elegans* nephrocystins act as global
932 modifiers of cilium structure. *The Journal of Cell Biology* **180**, 973-988 (2008).

933

934

935
936 55. Louie CM, Gleeson JG. Genetic basis of Joubert syndrome and related disorders of cerebellar
937 development. *Human molecular genetics* **14 Spec No. 2**, R235-242 (2005).

938
939 56. Matsui H, Namikawa K, Babaryka A, Koster RW. Functional regionalization of the teleost
940 cerebellum analyzed in vivo. *Proceedings of the National Academy of Sciences of the United
941 States of America* **111**, 11846-11851 (2014).

942
943 57. Kimmel CB, Ballard WW, Kimmel SR, Ullmann B, Schilling TF. Stages of embryonic
944 development of the zebrafish. *Dev Dyn* **203**, 253-310 (1995).

945
946 58. Sander JD, *et al.* Targeted gene disruption in somatic zebrafish cells using engineered
947 TALENs. *Nat Biotechnol* **29**, 697-698 (2011).

948
949 59. Pan YA, *et al.* Zebrabow: multispectral cell labeling for cell tracing and lineage analysis in
950 zebrafish. *Development* **140**, 2835-2846 (2013).

951
952 60. Pan YA, Choy M, Prober DA, Schier AF. Robo2 determines subtype-specific axonal
953 projections of trigeminal sensory neurons. *Development* **139**, 591-600 (2012).

954
955 61. Schindelin J, *et al.* Fiji: an open-source platform for biological-image analysis. *Nat Methods*
956 **9**, 676-682 (2012).

957
958 62. Lauter G, Soll I, Hauptmann G. Multicolor fluorescent in situ hybridization to define
959 abutting and overlapping gene expression in the embryonic zebrafish brain. *Neural Dev* **6**,
960 10 (2011).

961
962 63. Randlett O, *et al.* Whole-brain activity mapping onto a zebrafish brain atlas. *Nature Methods*
963 **12**, 1039-1046 (2015).

964
965 64. Sklavos S, Dimitrova DM, Goldberg SJ, Porrill J, Dean P. Long time-constant behavior of the
966 oculomotor plant in barbiturate-anesthetized primate. *J Neurophysiol* **95**, 774-782 (2006).

967
968 65. Miri A, Daie K, Arrenberg AB, Baier H, Aksay E, Tank DW. Spatial gradients and
969 multidimensional dynamics in a neural integrator circuit. *Nat Neurosci* **14**, 1150-1159
970 (2011).

971
972 66. Kawashima T, Zwart MF, Yang CT, Mensh BD, Ahrens MB. The Serotonergic System Tracks
973 the Outcomes of Actions to Mediate Short-Term Motor Learning. *Cell* **167**, 933-946 e920
974 (2016).

975
976 67. Ross LS, Parrett T, Easter SS, Jr. Axonogenesis and morphogenesis in the embryonic
977 zebrafish brain. *J Neurosci* **12**, 467-482 (1992).

978
979 68. Fox MA, Sanes JR. Synaptotagmin I and II are present in distinct subsets of central synapses.
980 *J Comp Neurol* **503**, 280-296 (2007).

981
982 69. Higashijima S, Hotta Y, Okamoto H. Visualization of cranial motor neurons in live transgenic
983 zebrafish expressing green fluorescent protein under the control of the islet-1
984 promoter/enhancer. *J Neurosci* **20**, 206-218 (2000).

985
986

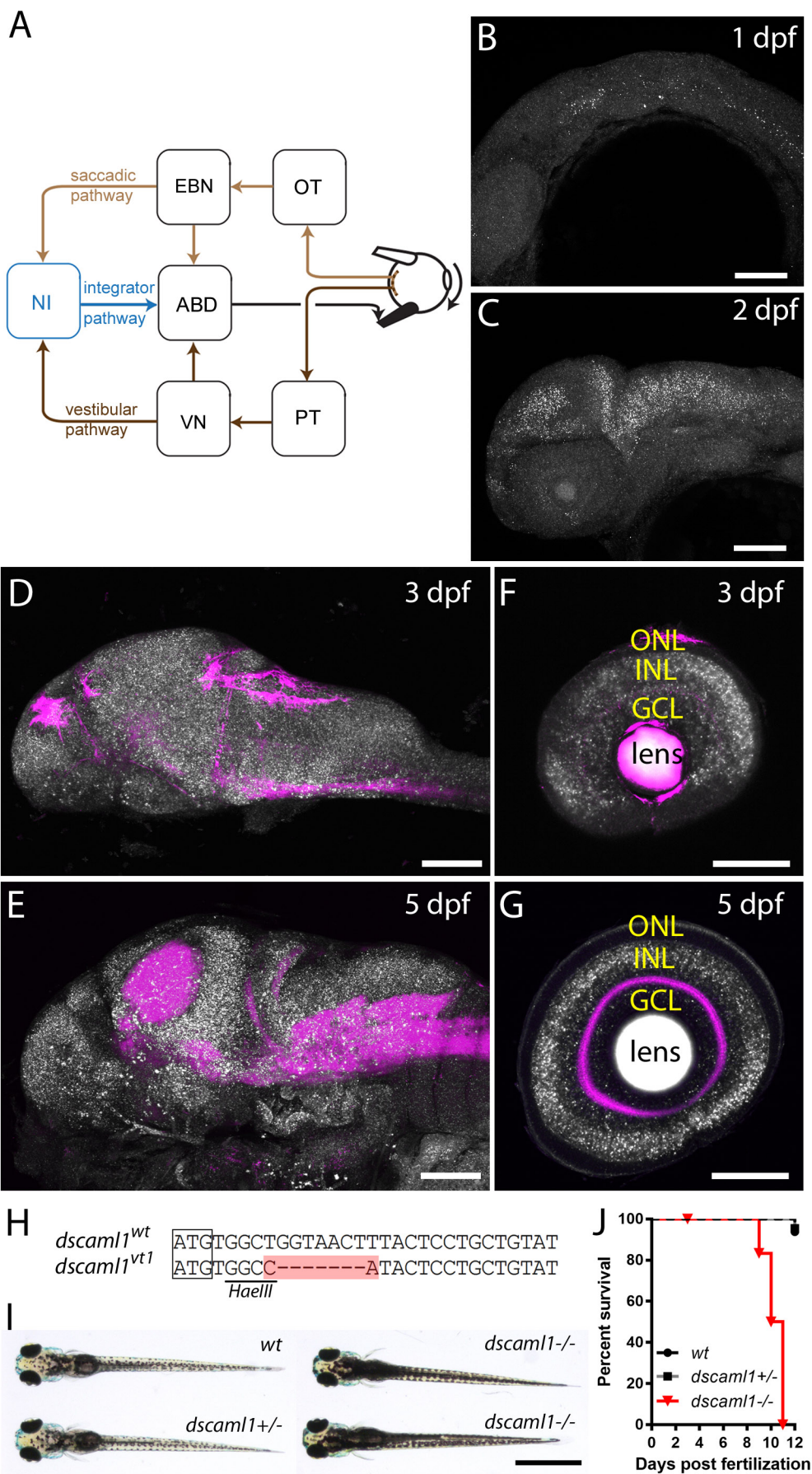


Figure 1.

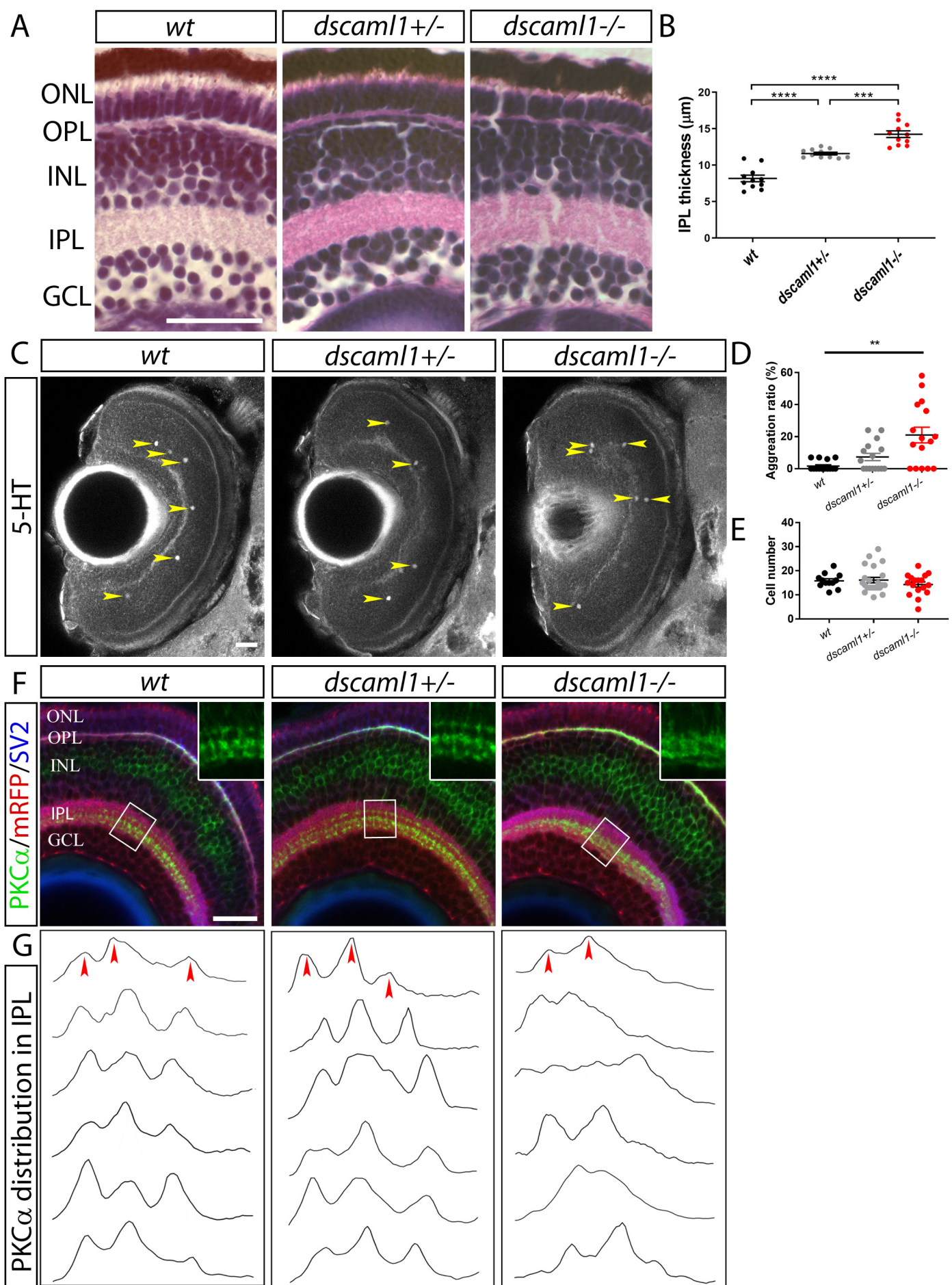


Figure 2

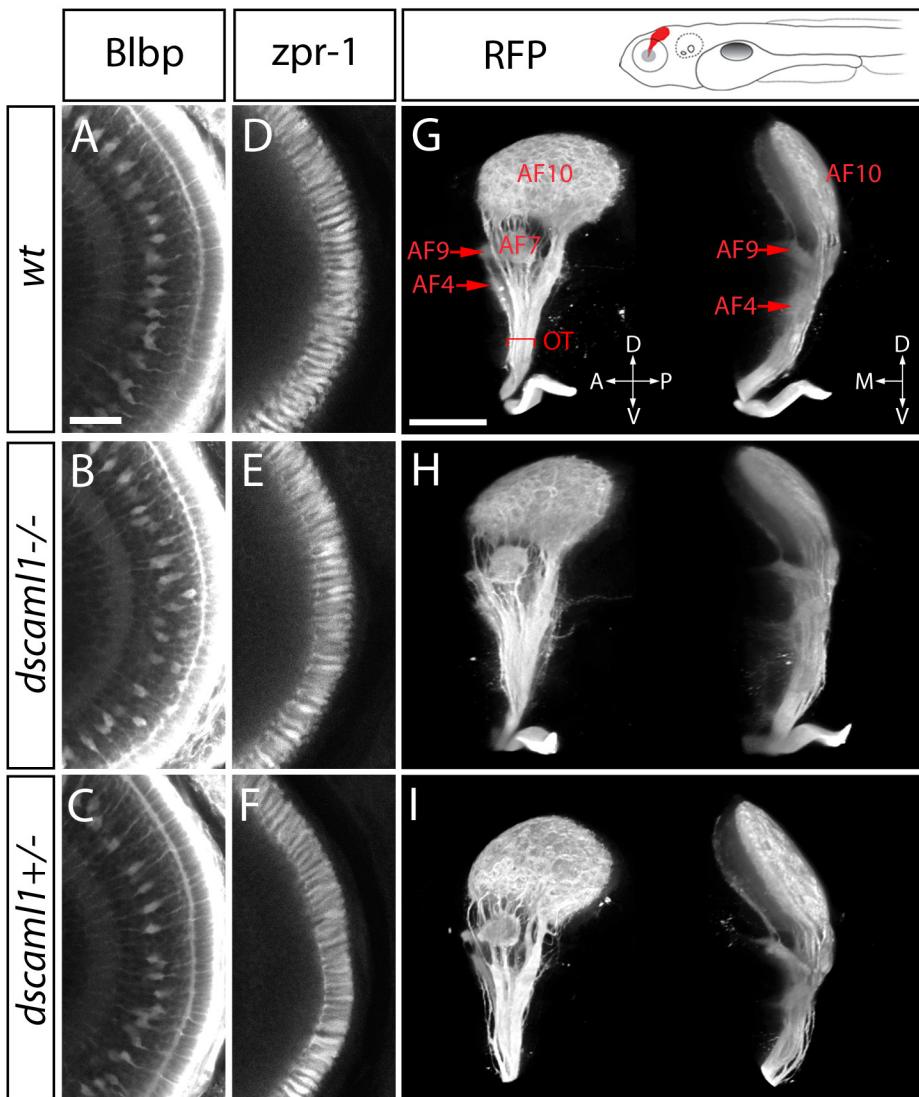


Figure 3

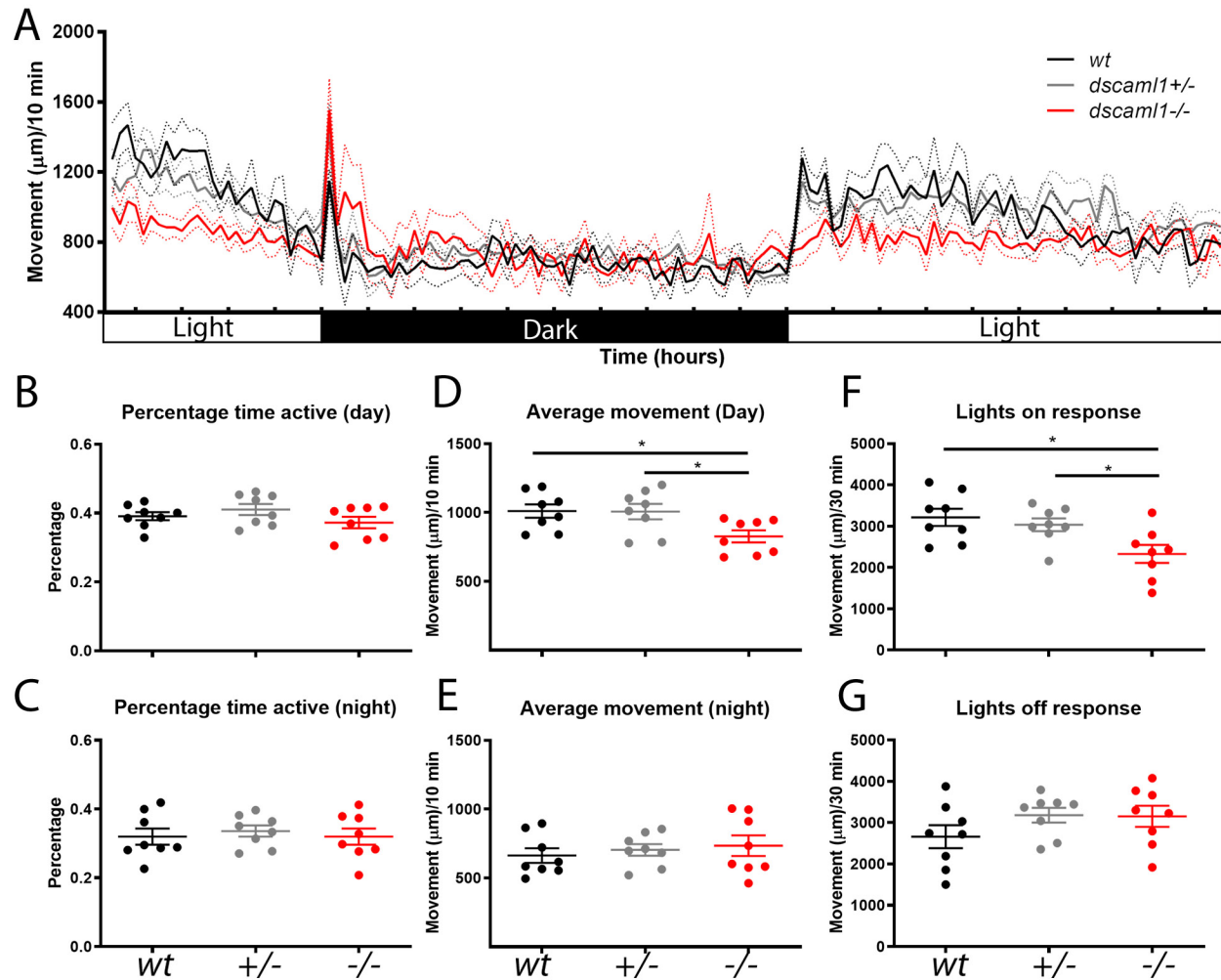


Figure 4

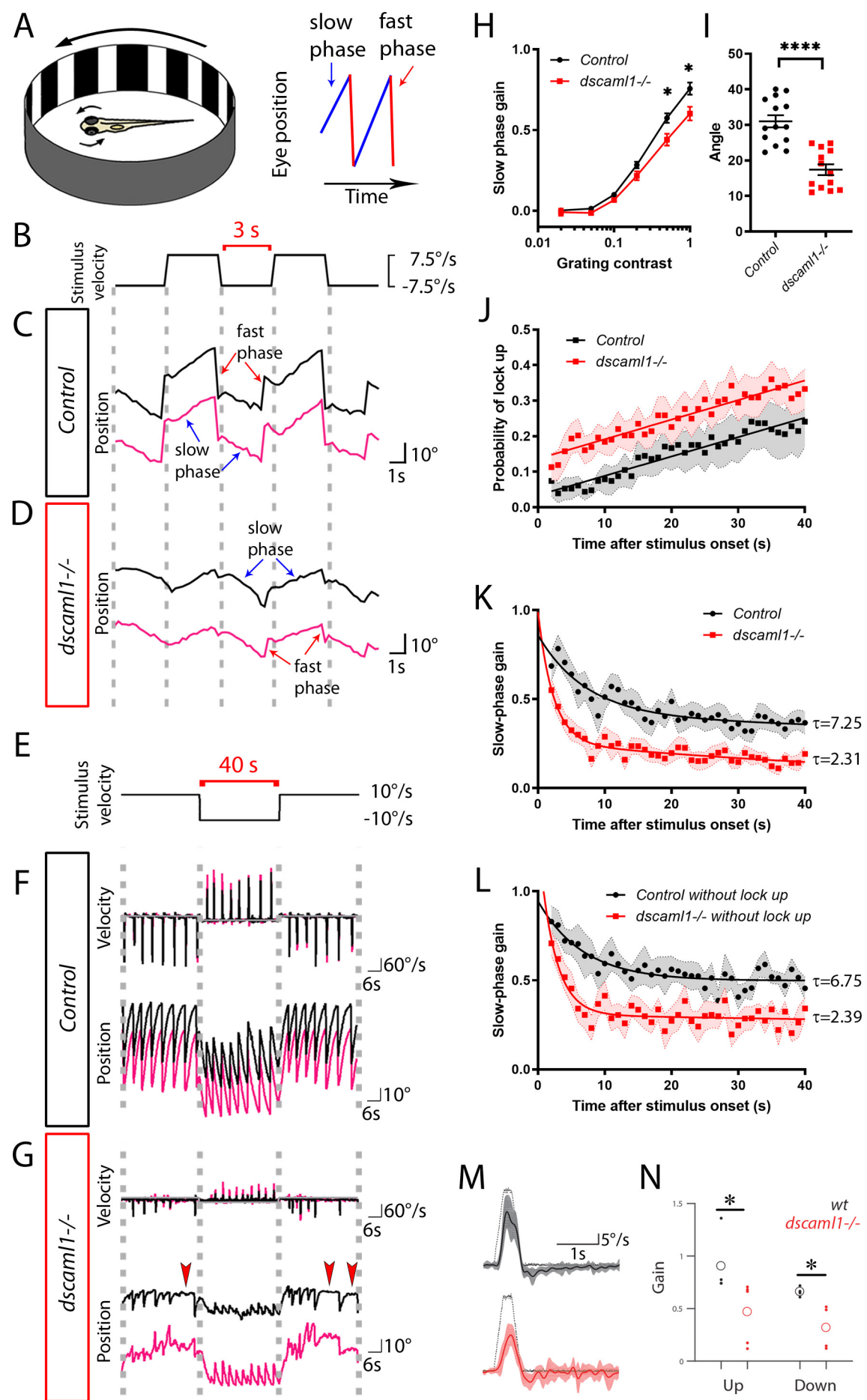


Figure 5

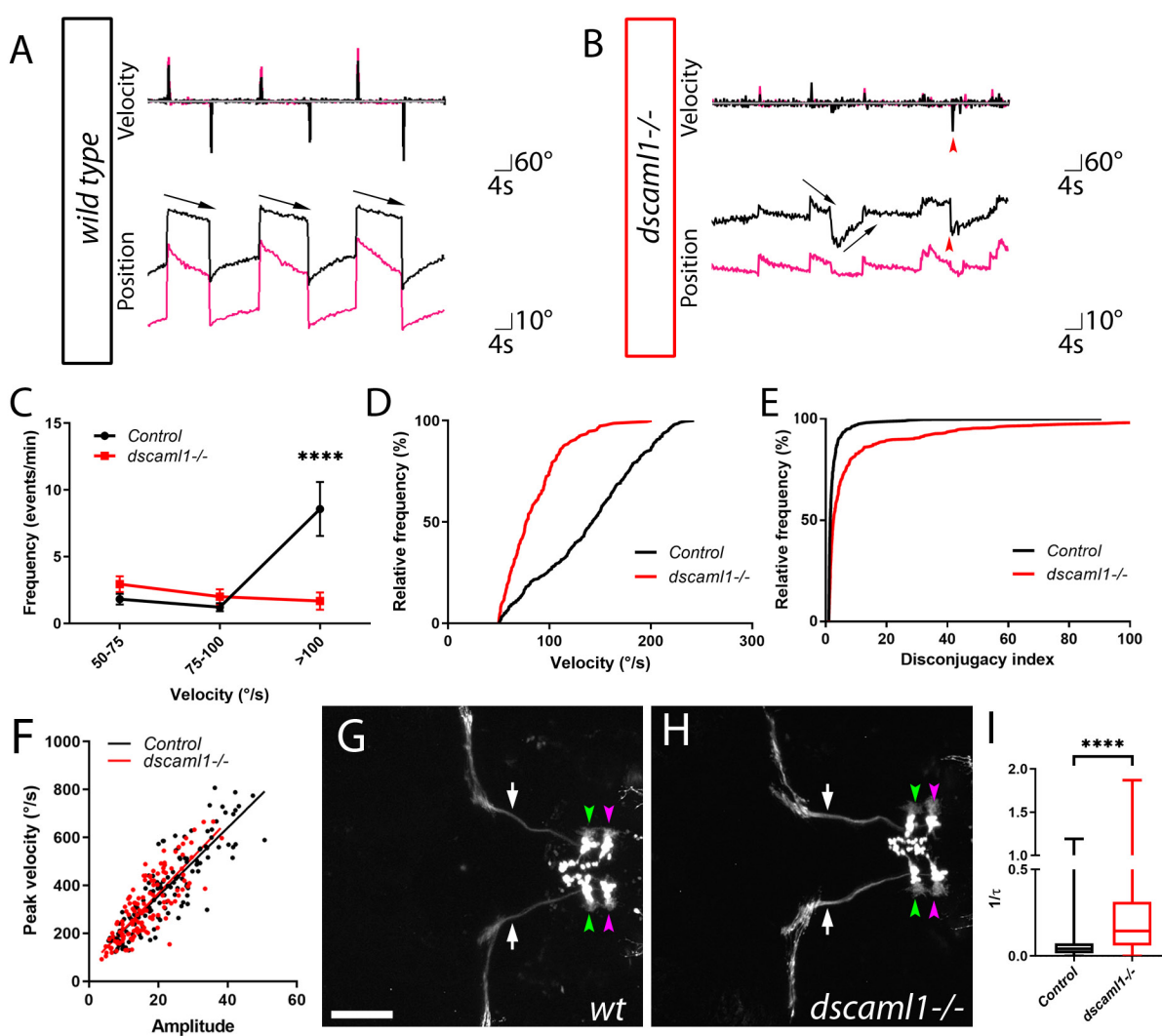


Figure 6

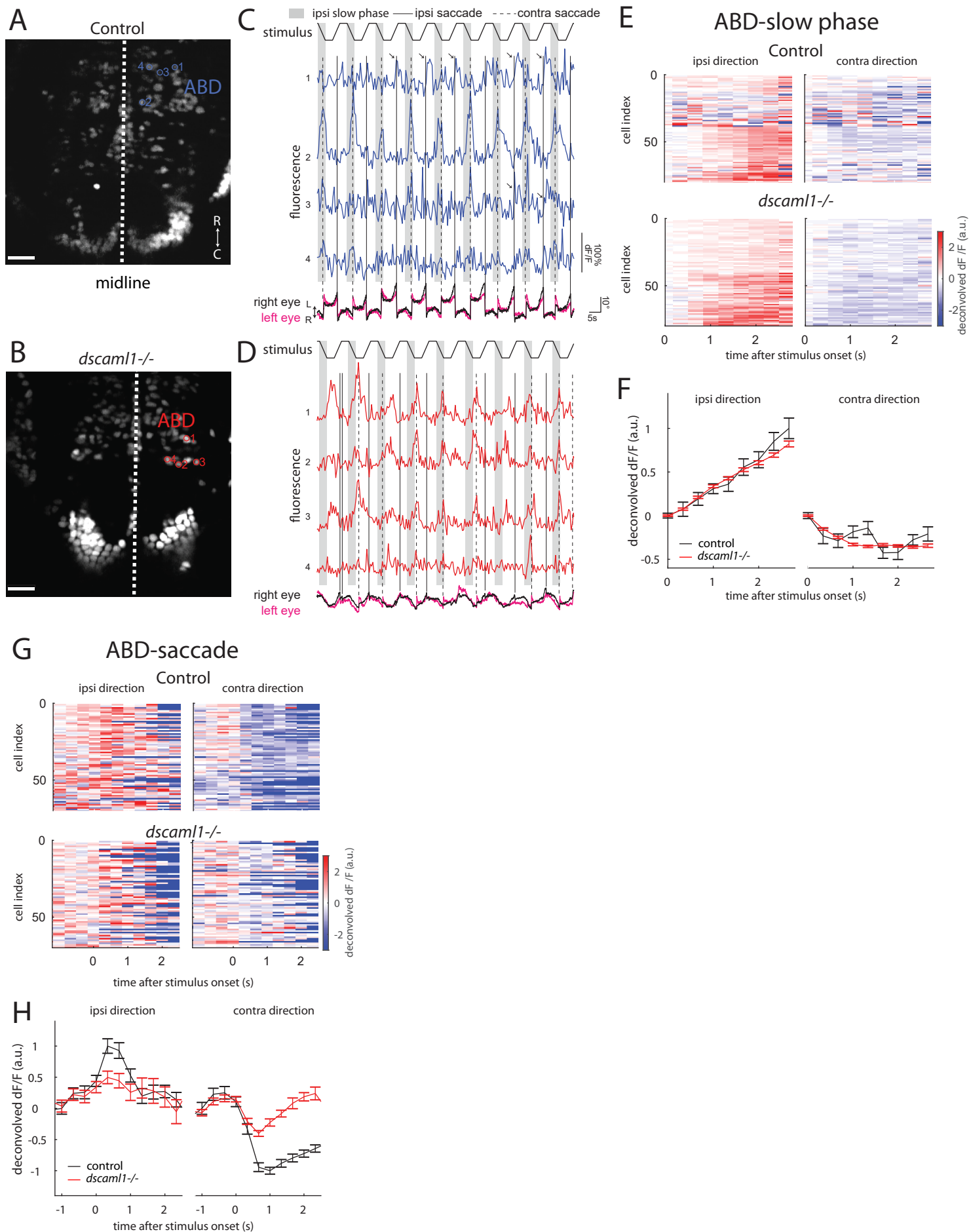
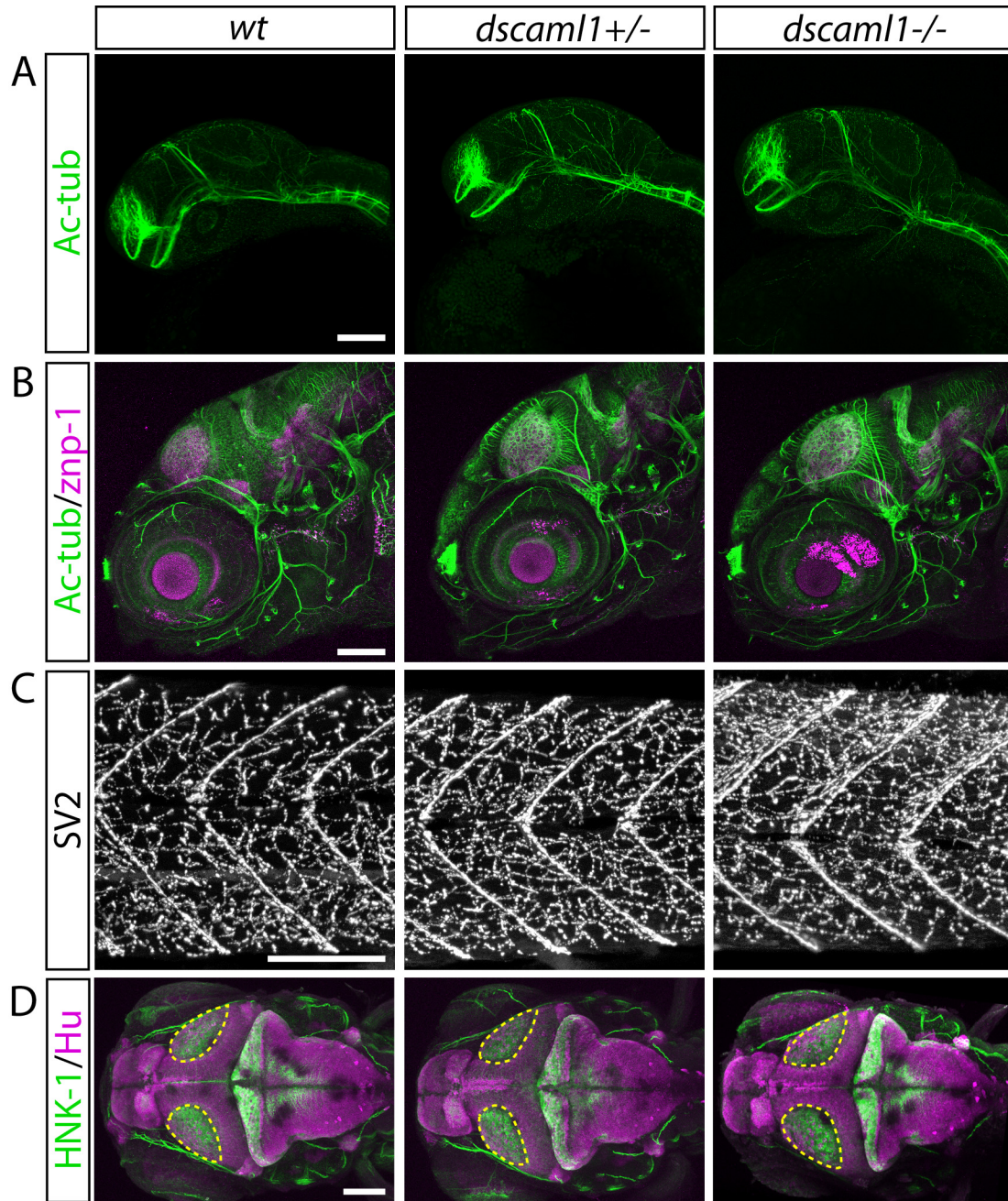
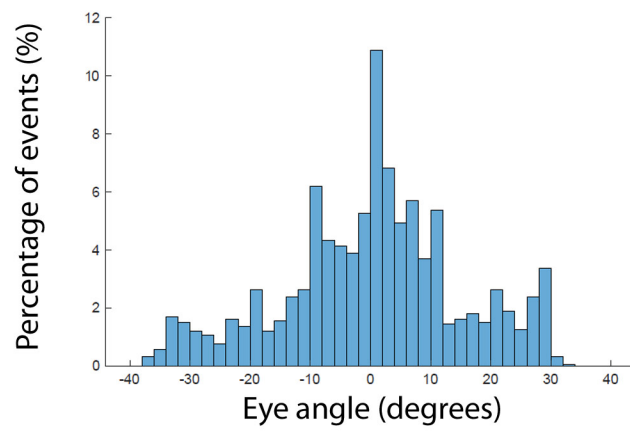


Figure 7



Supplementary Figure S1



Supplementary Figure S2

With lock up	Control	<i>dscaml1-/-</i>
Y ₀	0.86	0.99
Contribution of long component	47.31	25.87
Tau (short)	7.25	2.31
Tau (long)	305.00	72.01

Without lock up	Control	<i>dscaml1-/-</i>
Y ₀	0.9461	1.297
Contribution of long component	52.66	23.65
Tau (short)	6.749	2.385
Tau (long)	2.89E+08	472.4

Table I. Double exponential decay fit for slow phase gain.